eNeuro

Research Article: Methods/New Tools | Novel Tools and Methods

Fluorescence-based quantitative synapse analysis for cell-type specific connectomics

https://doi.org/10.1523/ENEURO.0193-19.2019

Cite as: eNeuro 2019; 10.1523/ENEURO.0193-19.2019

Received: 17 May 2019
Revised: 8 August 2019
Accepted: 11 September 2019

Title: Fluorescence-based quantitative synapse analysis for cell-type specific connectomics

Abbreviated title: Quantitative cell-type specific connectomics

Names and author affiliations: Dika A. Kuljis, Eunsol Park, Cheryl A. Telmer, Jiseok Lee, Daniel S. Ackerman, Marcel P. Bruchez, and Alison L. Barth
Department of Biological Sciences, Carnegie Mellon University, Pittsburgh, PA, USA

Corresponding author information:
Professor Alison L. Barth
159C Mellon Institute
Department of Biological Sciences and Center for Neural Basis of Cognition
Carnegie Mellon University
4400 Fifth Avenue
Pittsburgh, PA 15213
Phone: 412-268-1198
Fax: 412-268-8423
Email: barth@cmu.edu

Author Contributions:
DAK was responsible for all aspects of the *in vivo* construct expression and quantitative synaptic analysis and writing of the manuscript. EP contributed to synaptic quantitation and input analysis. CAT was responsible for design and generation of FAPpost constructs. JL performed in vivo imaging. DSA contributed to the cloning of Cre-dependent AAV vectors. MPB was responsible for design and creation of the postsynaptic targeting constructs and contributed to fluorescence image analysis, and manuscript preparation. ALB was responsible for construct and experimental design, data acquisition and analysis, and writing of the manuscript.

Number of Figures and Tables:
7 Figures
1 Table
5 Extended Figures

Word count:
Abstract: 210 words
Introduction: 634 words
Discussion: 1837 words

Funding sources: This work was supported by the Kaufman Foundation (to ALB and MPB), NIH R21 NS092019 (to MPB and ALB), NIH RF1 MH114103 (to MPB and ALB), and NIH T32 NS 086749 (to DAK).

Conflict of interest: MPB is a founder and shareholder in Sharp Edge Labs, a company that licensed and is commercially utilizing the FAP-Fluorogen technology.

Abstract

Anatomical methods for determining cell-type specific connectivity are essential to inspire and constrain our understanding of neural circuit function. We developed genetically-encoded reagents for fluorescence-synapse labeling and connectivity analysis in brain tissue, using a fluorogen-activating protein (FAP)- or YFP-coupled, postsynaptically-localized neuroligin-1 targeting sequence (FAP/YFPpost). FAPpost expression did not alter mEPSC or mIPSC properties. Sparse AAV-mediated expression of FAP/YFPpost with the cell-filling, red fluorophore dTomato (dTom) enabled high-throughput, compartment-specific detection of putative synapses across diverse neuron types in mouse somatosensory cortex. We took advantage of the bright, far-red emission of FAPpost puncta for multichannel fluorescence alignment of dendrites, FAPpost puncta, and presynaptic neurites in transgenic mice with saturated labeling of parvalbumin (PV), somatostatin (SST) or vasoactive intestinal peptide (VIP)-expressing neurons using Cre-reporter driven expression of YFP. Subtype-specific inhibitory connectivity onto L2 neocortical pyramidal (Pyr) neurons was assessed using automated puncta detection and neurite apposition. Quantitative and compartment-specific comparisons show that PV inputs are the predominant source of inhibition at both the soma and the dendrites and were particularly concentrated at the primary apical dendrite. SST inputs were interleaved with PV inputs at all secondary- and higher-order dendritic branches. These fluorescence-based synapse labeling reagents can facilitate large-scale and cell-type specific quantitation of changes in synaptic connectivity across development, learning, and disease states.

Significance Statement

High-throughput quantitation of synapse number and distribution can reveal principles of circuit function and their adaptive or pathological alterations. Molecular genetic, fluorescence-based approaches targeted to discrete cell types can enable automated detection and quantification of input-specific synapses in complex brain tissues. In addition, these tools present a low barrier to use within

69 the neuroscience community through volumetric confocal analysis of tissue specimens. Here we
70 evaluate inhibitory synapse distribution across layer 2 (L2) pyramidal neurons using postsynaptic
71 expression of a previously characterized, neuroligin-based construct. We find that inhibitory inputs
72 from fluorescently-labeled parvalbumin and somatostatin neurons are intermingled across the
73 proximal dendrites, and that inputs from vasoactive-intestinal peptide neurons are rare for L2
74 pyramidal neurons.

3

Introduction

The organization, number, and input identity of synapses onto a cell are critical determinants of neuronal activity. Although electrophysiological analyses of synaptic properties have provided a rich framework to build and test hypotheses about neural computations during sensation and behavior, these analyses cannot reveal broader principles of synaptic distribution across the neuron. Since alterations to synaptic function in select circuits and cell types are associated with autism, intellectual disability, psychiatric, and neurologic disease (Bayes et al., 2011; Sudhof, 2017), quantitative metrics about synaptic location, size, and input specificity are likely to provide key insights into how neural circuits are related to disease pathology.

Electron-microscopy (EM) provides nanometer resolution for ultrastructural identification of synaptic contacts and has been employed for brain-area and cell-type quantitative analysis (Bock et al., 2011; Briggman et al., 2011; Chandrasekaran et al., 2015; Kim et al., 2014); however, EM is hampered by technical demands of sample preparation, imaging time, data storage, and labor-intensive analysis that make comparisons across multiple individuals or conditions difficult. Recent studies have attempted to use EM for quantitative analysis of synapse organization between defined pre- and postsynaptic partners, but these computationally-intensive approaches are difficult to adopt and scale for broad use (Glausier et al., 2017; Kornfeld et al., 2017; Kubota et al., 2015; Vishwanathan et al., 2017). Fluorescence-based microscopy methods are an attractive alternative to EM, because light-microscopy facilitates faster acquisition of larger tissue volumes and enables use of spectrally distinct, genetically encoded fluorophores for discrimination of molecularly diverse cells and synapse types.

There has been great interest in developing tools and methodologies for synapse labeling using molecular, genetic, or histochemical techniques for light microscopy, including GFP-tagging synaptic molecules, GFP reconstitution across synaptic partners (GRASP) and array tomography (Chen et al., 2012; Fortin et al., 2014; Gross et al., 2013; Kim et al., 2011; Kinoshita et al., 2019;

100 Martell et al., 2016; Micheva and Smith, 2007; Villa et al., 2016b). Fluorescence-based, sparse
101 labeling of post-synaptic neurons in intact brain tissue has been especially helpful in this regard, as it
102 reduces the analysis bottleneck that arises from broadscale immunohistochemical labeling of
103 synapses from neurons intermingled in the analysis volume. However, high-throughput/volumetric
104 synaptic analysis for individual neurons has not yet become routine, possibly due to low signal-to-
105 noise and synaptogenesis or abnormal synapse stabilization associated with overexpression of
106 synaptic tags (El-Husseini et al., 2000; Kim et al., 2011; Martell et al., 2016; Tsetsenis et al., 2014).
107 We sought to develop molecular genetic tools for comprehensive fluorescence labeling of
108 postsynaptic sites across an individual neuron, in a complex tissue environment. We employed
109 fluorogen-activating protein (FAP), a modified antibody fragment that emits in the far red upon
110 binding of a small molecule ligand, a derivative of malachite green (MG; Szent-Gyorgyi et al., 2013),
111 targeted to postsynaptic sites using the well-validated post-synaptic tag derived from the
112 transmembrane and cytoplasmic region of mouse neuroligin-1 (NL-1) (Druckmann et al., 2014; Kim
113 et al., 2011; Kwon et al., 2018).
114 Sparse, virus-mediated coexpression of FAPpost with the cell-filling fluorophore dTomato
115 (dTom) showed broad, punctate labeling across distinct pyramidal cell compartments. Aided by
116 automated image analysis, we quantitatively evaluated the distribution of inhibitory synapses
117 identified from analysis of more than 90,000 synaptic puncta in neocortical pyramidal (Pyr) neurons
118 in superficial layers of somatosensory cortex. Using comprehensive fluorescence-labeling of cell-
119 type specific neurites in parvalbumin (PV), somatostatin (SST), and vasoactive intestinal peptide
120 (VIP) Cre-driver transgenic mice allowed us to align FAPpost puncta to quantify inhibitory inputs for
121 L2 Pyr neurons. This quantitative analysis revealed that PV inputs dominated the soma and the
122 synapse-dense 1° apical dendrite, and that PV inputs had a moderately higher density than SST inputs
123 across all L2 dendrites. VIP neurons only sparsely innervated L2 Pyr neurons. These studies help

5

124 establish a framework for a high-throughput analysis of synapse organization in brain tissue during
125 health and disease.

126 **Materials and Methods**

127 All experimental procedures were conducted in accordance with the NIH guidelines and were
128 approved by the Institutional Animal Care and Use Committee at Carnegie Mellon University.

129 **Construct Design**

130 **FAPpost Cloning**

131 To make the plasmid for packaging into AAV, post-mGRASP from Addgene (#34912 -
132 paavCAG-post-mGRASP-2A-dTom) was modified by annealing oligos and inserting into BamHI
133 and XhoI digested backbone to introduce an AgeI site (PostBamXhoF 5'GATCC CTT ACCGGT
134 ATC TTA C and PostBamXhoR 5' TCGAG TAA GAT ACCGGT AAG G). PCR was used to
135 produce the Igkappa leader sequence, cmyc epitope and dL5** FAP (Szent-Gyorgyi et al., 2008;
136 Szent-Gyorgyi et al., 2013; Telmer et al., 2015) for introduction into the BamHI and AgeI of the
137 modified backbone (BamKappaF 5' TATATA GGATCC ggcttggggatatccaccatgg and dL5AgeSfiR
138 5' TATATA ACCGGT ACCTCC ggccagaccggccgc GGAGAG). The BamHI/HindIII fragment was
139 moved to create pENN.AAV.hSyn.kappa.myc.dL5.POSTsyn.T2A.dTom.WPRE.BGH (Addgene
140 FAPpost plasmid ID 105981). AAV1 serotype was produced by Penn Vector Core.

141 **Fl-YFPpost and fl-FAPpost Cloning**

142 For Cre-inducible expression, the kappa.myc.dL5.POSTsyn.T2A.dTom region was PCR
143 amplified with primers containing BsrG1 and KpnI restriction sites (partial KpnI digestion was
144 required) and ligated into digested pAAV-FLEX (fl; generous gift from Oliver Schluter) to produce
145 pAAV-FLEX-hSyn-kappa-myc-dL5-POSTsyn-T2A.dTom-WPRE-SV40. PCR amplification was
146 used to generate the SYFP2 (YFP) (Kremers et al., 2006) coding fragment (iGEM BBa_K864100)
147 that was then SfiI digested to replace the FAP in the pAAV-FLEX resulting in pAAV-FLEX-hSyn-

148 kappa-myc-dL5-POSTsyn-T2A-dTom-WPRE-SV40 (Addgene fl-FAPpost plasmid ID 105982;
149 Addgene fl-YFPpost plasmid ID 105983). Constructs were packaged into AAV1 and produced by
150 Penn Vector Core.

151 **Animals**

152 Experiments were performed on wild-type and transgenic reporter male and female mice on a
153 C57BL6J background (Table 1). Cre recombinase lines used included Emx1-IRES-Cre (Jackson
154 Labs stock #005628, Pvalb-2A-Cre (Jackson Labs stock # 008069; (Hippenmeyer et al., 2005)), SST-
155 IRES-Cre (Jackson Labs stock # 013044; (Taniguchi et al., 2011) and VIP-IRES-Cre (Jackson Labs
156 stock # 010908; (Taniguchi et al., 2011)). Homozygous Cre-expressing mice were mated with
157 homozygous Ai3 mice (Jackson Labs Stock # 007903) to create heterozygous transgenic mice with
158 eYFP- (YFP)-labeled SST, PV, or VIP interneurons. Pyr cells from at least three mice from each line
159 were used to characterize FAPpost expression patterns.

160 **Virus injection surgery**

161 FAPpost virus (0.4 µL) was stereotaxically injected into barrel cortex through a small
162 craniotomy (bregma -0.9, lateral 3.00, depth 0.5 mm) in isoflurane-anaesthetized mice aged postnatal
163 day (P12-17) using a Hamilton syringe (Hamilton; Reno, NV), Stoelting infusion pump 597
164 (Stoelting; Wood Dale, IL, Model #53210), and custom injection cannulas (Plastics One; 598
165 Phoenix, AZ). Mice were treated once with ketofen (5 mg/kg, Sigma-Aldrich; 599 St. Louis, MO),
166 then allowed to recover in their home cage until weaning (P21),when they were moved to a new cage
167 with their littermates.

168 **Fixed tissue preparation and immunohistochemistry**

169 Seven to 15 days following virus injection, animals were anesthetized with isoflurane and
170 transcardially perfused at mid-day using 20 mL phosphate buffered saline (PBS; pH 7.4) followed by
171 20 mL 4% paraformaldehyde in PBS (PFA; pH 7.4). Brains were removed, and postfixed overnight

7

172 at 4°C in 4% PFA before transfer into 30% sucrose cryoprotectant. After osmotic equilibration brains
173 were sectioned (50µm thick section) using a freezing-microtome.
174 Free-floating brain sections containing dTom-expressing cells were washed using PBS before
175 30 minute room temperature incubation with malachite green (MG) dye (300nM in PBS; (Pratt et al.,
176 2017)). MG-dyed sections were then rinsed with PBS before mounting on glass microscope slides
177 with Vectashield fluorescent mounting media (Vector Lab; Burlingame, CA). Before MG dye
178 application, a subset of brain sections underwent immunofluorescence staining. Brain sections from
179 PV-Cre, SST-Cre, or VIP-Cre x Ai3 for saturated cell-type specific YFP labeling underwent GFP
180 immunofluorescence staining to enhance YFP signal. These sections were first blocked (10% NGS,
181 0.1% TritonX, 0.1M PBS), and incubated for 48 hour at 4°C with anti-chicken GFP primary antibody
182 (1:2000 dilution in blocking solution; Abcam AB13970; Cambridge, MA). Sections were rinsed with
183 PBS, then incubated with Alexa488 anti-chicken secondary antibody (1:500, in blocking solution;
184 Invitrogen A-11039; Carlsbad, CA). In the same manner, a subset of PV-Cre x Ai3 brain sections
185 underwent bassoon immunofluorescence staining to visualize presynaptic release sites. These
186 sections were blocked (10% DS, 0.2% TritonX, 0.1M PBS), then incubated overnight at 4°C with
187 mouse anti-bassoon primary antibody (1:1500 in blocking solution; Enzo Life Sciences Assay Design
188 VAM-PS003). Slices were rinsed with 0.2%PBST then incubated with Alexa405 anti-mouse
189 secondary antibody (1:500 dilution in blocking solution; Invitrogen A-31553).

190 **Confocal Imaging**

191 FAPpost expression in L2/3 (~200-300µm below the pial surface) of the S1 barrelfield (S1BF)
192 was confirmed by the presence of layer 4 barrels. Pyr cells were identified using morphological
193 criteria, including the presence of a thick apical dendrite oriented toward the pial surface, pyramidal-
194 shaped cell body, laterally projecting basal dendrites, a descending axon identified by its narrow
195 diameter, and the ubiquitous presence of dendritic spines, particularly on higher-order branches. Only
196 isolated Pyr cells (typically at the edge of the viral transduction zone) that exhibited dendritic dTom

197 as well as punctate FAP signal were selected for imaging and quantitation. FAPpost and dTom
198 expression were not always positively correlated, an effect that was unexpected given the construct
199 design. dTom-expressing neurons that did not exhibit membrane-localized FAP fluorescence, or
200 showed diffuse and low-intensity signal were excluded from analysis. Analyzed cells showed no
201 significant relationship between FAPpost puncta intensity and calculated puncta density along the
202 dendrite. In almost all cases, selected cells included the entire soma in the image dataset. Because
203 cortical dendrites are > 200µm long and could lie outside the imaged area, only a fraction of the
204 dendritic arbor was collected and analyzed.

205 Sections were observed under a LSM 880 AxioObserver Microscope (Zeiss), using 63x oil-
206 immersion objective lens (Plan-Apochromat, 1.40 Oil DIC M27) with the pinhole set at 1.0 Airy disk
207 unit. Maximum image size was 1024 x1024 pixels. Zoom factor was set to 1, corresponding to a
208 voxel dimension of 0.13µm x 0.13µm x 0.32µm in X, Y, and Z directions. Selected cell bodies were
209 centered in the field of view (135µm x 135µm). Up to 100 images with a Z-interval of 0.32µm and
210 50% overlap between optical sections were acquired per stack. Fluorescence acquisition settings were
211 as follows: Alexa405 (excitation λ405, emission λ452, detection λ406-498), Alexa488
212 (excitation λ488, emission λ504, detection λ490-517), YFP (excitation λ514, emission λ535,
213 detection λ517-535), dTom (excitation λ561, emission λ579, detection λ561-597), MG/FAP
214 (excitation λ633, emission λ668, detection λ641-695). Optimal laser intensities for each channel
215 were set for each cell independently, and images were collected to avoid pixel saturation. Well-
216 isolated cells of interest were centered in the image frame and the Z-stack dimensions were set
217 manually by tracking dTom labeled dendrites. Z-stacks typically ranged from 30-40µm for a given
218 neuron. For experiments assessing bassoon immunofluorescence alignment with YFP-expressing PV
219 neurites and FAPpost puncta on soma of transduced cells, image size was 1912 x 1912 pixels with a
220 zoom factor was set to 2, corresponding to a voxel dimension of 0.05µm x 0.05µm x 0.32µm in X, Y,

221 and Z directions. The total Z-stack depth typically ranged between 10-15µm starting from the brain
222 section surface, where bassoon antibody penetration was most complete.

223 **Cranial window construction for *in vivo* imaging**

224 One week after virus injection, mice were isoflurane anesthetized and heads fixed using a
225 custom-made nose clamp. Eyes were covered with ointment, hair was removed with Nair, and scalp
226 was disinfected with povidone iodine. Scalp and periosteum was removed, and skull surface
227 roughened by scraping with a slowly rotating dental drill. A thin layer of Krazyglue was applied to
228 the skull before a custom-made head bracket was attached in the right hemisphere using Krazyglue
229 and dental cement (Lang Dental, 1223PNK). The skull was carefully thinned around a 3mm diameter
230 circle centered above the left hemisphere S1BF using a dental drill (Dentsply, 780044). After
231 extensive thinning, the loose bone flap was detached using a microforcep. A glass window composed
232 of 3mm diameter glass (Harvard Apparatus, 64-0720) attached to 5 mm diameter glass (Harvard
233 Apparatus, 64-0700) was mounted above the exposed brain. The window was sealed with 3MTM
234 VetbondTM. A chamber wall was built around the window with dental cement. Ketoprofen (3
235 mg/Kg) was given subcutaneously.

236 **Two-photon imaging**

237 Mice were anesthetized with 1.5 % isoflurane and mounted under a Femtonics FEMTO2D
238 microscope. Layer 1/2 dendrites expressing dTom and YFPpost were visualized under a 63x
239 objective using 950 nm excitation (Spectra-Physics Mai Tai HP; Santa Clara, CA) with simultaneous
240 detection of dTomato and YFPpost using red and green PMTs, respectively. Single-plane 60x60µm
241 (1000x1000 pixel) linescan (15x averaging) images were acquired using MES software (Femtonics,
242 v.5.2878). The raw intensity matrix for each channel was converted to a grayscale image in
243 MATLAB (MathWorks, R2017a). Channels were overlaid and brightness/contrast adjusted using
244 Photoshop 6.0 (Adobe).

245 **Electrophysiology**

246 FAPpost-injected mice were sacrificed at age P20-25 by brief isoflurane anesthesia and
247 decapitation. Coronal slices (350µm thick) were prepared in regular ice-cold artificial cerebrospinal
248 fluid (ACSF) composed of (in mM): 119 NaCl, 2.5 KCl, 1 NaH_2PO_4, 26.2 $NaHCO_3$, 11 glucose, 1.3
249 $MgSO_4$, and 2.5 $CaCl_2$ equilibrated with 95%/5% O_2/CO_2. Slices recovered in the dark at room
250 temperature for 60 minutes before transfer to an electrophysiology rig where they were perfused with
251 ACSF containing 1µM tetrodotoxin (Tocris, UK) to silence spontaneous activity. The injection site
252 was identified by dTom fluorescent cell bodies using an Olympus light microscope (BX51WI). Pyr-
253 targeted recordings (4-5 animals per group) were done in the absence of MG dye, since we were
254 interested in whether *in vivo* expression of the FAPpost construct would influence synaptic function
255 and MG was never applied before tissue fixation for anatomical analysis. Borosilicate glass electrode
256 resistance was 4-8 MΩ. Electrode internal solution was composed of (in mM): 130 cesium
257 gluconate, 20 HEPES, 0.4 EGTA, 2.8 NaCl, 5 Tetraethylammonium chloride (TEA-Cl), 4 Mg-ATP
258 and 0.3 Na-GTP, pH 7.25-7.30, 280-290 mOsm. Trace amounts of AlexaFluor488 were included in
259 the internal solution to confirm that targeted cells had pyramidal-like morphologies.
260 Electrophysiological data were acquired using a Multiclamp 700B amplifier (Axon Instruments;
261 Foster City, CA) and a National Instruments acquisition interface (National Instruments; Austin,
262 TX). The data were filtered at 3 kHz, digitized at 10 kHz and collected by Igor Pro 6.0 (Wavemetrics;
263 Lake Oswego, Oregon). After forming a GΩ seal, negative pressure was applied to the cell to enter
264 whole-cell mode, and following 2-3 minutes acclimation time, miniature excitatory postsynaptic
265 currents (mEPSCs) were collected at -70 mV holding potential for 5 minutes. Holding potential was
266 slowly raised to 0 mV over an additional minute, and following 1 minute acclimation time, miniature
267 inhibitory postsynaptic currents (mIPSCs) were then collected. Traces were analyzed using
268 MiniAnalysis (Synaptosoft Inc., NJ), with a 7pA minimal amplitude cut-off. One hundred randomly
269 selected events for each cell (Pyr dTom- and dTom+) were used to create cumulative probability
270 histogram.

11

271 **Image analysis**

272 **Bassoon alignment**

273 PV-Cre x Ai3 mouse brain tissue sections containing FAPpost transduced cells were stained for
274 bassoon, a presynaptic marker of vesicle-release active zones that localizes to both excitatory and
275 inhibitory synapses (Richter et al., 1999). Images of the four different fluorescence channels
276 (bassoon, PV/YFP, dTom, FAPpost) were arranged side-by-side in series for all optical sections
277 containing the target soma. Analysis was restricted to the surface of a tissue section (~5 um from top)
278 where bassoon antibody penetration was complete. In deeper regions of the tissue section, bassoon
279 immunofluorescence was low to undetectable, making colocalization assessments unreliable.

280 First, bassoon puncta adjacent to the surface of a target dTom expressing soma were identified
281 by an experimenter. Bassoon puncta sometimes extended across multiple optical sections. Bassoon
282 colocalization at PV/YFP neurites was assessed by direct overlap of signal from the two channels.
283 FAPpost puncta at the soma surface were counted as being associated with bassoon when puncta
284 were aligned with <0.25 µm distance. A minimum of fifteen-bassoon puncta were assessed for
285 colocalization/alignment for each soma analyzed. We independently examined the rate of FAPpost
286 alignment with bassoon (to identify putative false positives) and PV, as well as PV alignment with
287 bassoon and FAPpost in the same manner.

288 To assess dendritic FAPpost alignment with synaptic immunofluorescence, spiny dendritic
289 segments running parallel to imaging plane (≥10µm in length) were manually assessed for alignment
290 between FAPpost and bassoon across one to five flattened confocal sections. Most FAPpost puncta
291 exhibited overlap with bassoon immunofluorescence within this sub-volume. Some FAPpost puncta
292 without an apparent bassoon partner could extend beyond the thin volume assessed. In this minority
293 of cases, additional adjacent optical sections at these specific locations were examined for bassoon
294 signal to determine whether these FAPpost puncta were actual false positives.

Imaris segmentation

Carl Zeiss image files were imported into Imaris version 8.4 equipped with the Filament Tracer plugin (Bitplane; Zurich, Switzerland). The dTom cell fill was used to create a 3D cell-surface rendering using a combination of surface and filament objects. FAPpost puncta were first reconstructed as 3D structures using "surface objects" (to outline puncta borders) created using an estimated 0.5µm diameter. Due to imaging limitations, only puncta larger than 3 voxels (~0.024µm^3) were counted, potentially undercounting very small synapses below this detection threshold. Large puncta that potentially reflected smaller, adjacent synapses were separated into multiple objects using the "split touching objects" function with the same estimated 0.5µm diameter. Thus, large puncta were potentially separated into multiple smaller synapses, a process that could increase the absolute number of detected synapses. Indeed, it is unclear for larger synapses whether these should be counted as a single synapse with multiple active sites and post-synaptic specializations (Tang et al., 2016), or combined into one large synapse (such as the giant synapses observed at the Calyx of Held). Puncta were digitally associated with the plasma membrane if their edges lay within 0.5µm from the soma surface or <1µm for spiny dendritic regions. Puncta 0.5µm below cell surface were attributed as cytosolic fluorescence and not included for analysis. Puncta "objects" were then converted into puncta "spots" (with automatic intensity max spot detection thresholds and a 0.5µm estimated-diameter) using "surface object" centroids in Imaris.

Puncta quantification

Puncta densities were quantified for different branch orders. Pyr neurons had only one apical branch segment that was then divided into higher-order branches. The number and length of 2° and higher-order branches analyzed could vary across cells, depending upon cell anatomy and image acquisition. For dendritic puncta density averages, values for the Pyr 1° apical dendrite were not included, because this compartment showed a significantly higher density and appeared to be a distinct compartment of the neuron that may be contiguous with the somatic compartment.

13

Automated input assignment

Presynaptic neurite reconstructions were created using automatic background subtraction thresholding of the presynaptic (PV, SST, or VIP) YFP channel, a split-touching objects diameter threshold of 1µm, and 6 voxel minimum area settings in Imaris. For confocal stacks where presynaptic neurite YFP signal exhibited z-axis related signal drop-off, neurite reconstructions using automatic settings were generated separately for superficial and deeper optical sections of the stack. In such cases, both sets of presynaptic neurite reconstructions were visually examined for comparable density and size profiles.

Puncta spots were assigned to a specific presynaptic input using a distance threshold of 0.15µm from spot centroid to the presynaptic neurite 3D-reconstructions edge. Methods using pre- and postsynaptic neurite colocalization may be confounded by false positives (where neurites are near the soma but do not synapse onto it) and false negatives (where a given neurite is associated with two or more postsynaptic sites that are conflated into a single crossing point). Indeed, in many cases, neurites made extended contacts with the soma surface that might include a single or multiple postsynaptic sites. We found that using postsynaptic puncta to differentiate multiple synapses along an extended region of presynaptic neurites enabled a more accurate estimate for the number of putative synaptic contacts (Figure 6).

Because distance parameters used to identify convergent signals could be digitally adjusted, we explored this space to establish a maximum distance for input detection of 0.15µm. This was below the diffraction limit for our confocal images. As expected, use of larger distance thresholds for detecting inputs resulted in a substantial increase in the number of assigned puncta. These values were out of range for other published values for inhibitory synapse density and provided confirmation that smaller distance thresholds were more stringent and likely to be more accurate.

Statistical Analysis

All reported values are mean ± SEM, unless otherwise stated. Dendritic puncta density is mean spot density per linear dendritic segment for a given cell. Soma density is total somatic spot count divided by soma surface area. Density distributions were tested for normality both within and across cells using the Shapiro-Wilk normality test. Within cells, all but two Pyr cells had normally distributed dendritic puncta densities. For these two cells, median dendritic puncta density was used to represent these cell's average dendritic puncta densities. Mean dendritic puncta density was used for all other cells. One-Way Repeated Measures (RM) ANOVA was used to detect dendritic segment-level dependent puncta density ($p < 0.05$). Pearson's correlation was employed to test the relationship between Pyr soma surface area and synapse density. Two-Way RM ANOVA was used to detect differences in the proportion of input-assigned synapses across Pyr compartments and input-types ($p < 0.05$). Post-hoc Tukey's multiple comparison testing was performed to identify significant group mean differences for anatomical data. For physiological data, unpaired Student's T-test was used to identify significant differences in mean mEPSC and mIPSC amplitude and frequency, and Kolmogorov-Smirnov test was used to test for differences in amplitude distributions ($p < 0.05$). All analyses were performed using Origin 2017 statistical software (OriginLab, Northampton, MA).

Results

FAPpost targeting to postsynaptic sites

Neuroligins are ubiquitously expressed at postsynaptic sites (Bemben et al., 2015). We took advantage of the pan-synaptic localization of a previously characterized NL-1 based tether (post mGRASP; (Druckmann et al., 2014; Kim et al., 2011; Kwon et al., 2018) to direct an extracellular fluorophore to postsynaptic sites. Because the trans-synaptic protein-protein interactions involved in GRASP and other protein complementation methods are irreversible and may be linked to synaptic stabilization (Scheiffele et al., 2000; Tsetsenis et al., 2014), we replaced post-mGRASP's extracellular GFP fragment with an intact FAP or YFP and packaged the modified construct into

15

368 recombinant AAV virus for expression under the control of the human synapsin promoter (Figure
369 1A,B). Virus was injected into mouse primary somatosensory (barrel) cortex for sparse neuronal
370 labeling (Figure 1C). Transduced cells were identified in fixed tissue specimens using both dTom
371 and FAP expression after MG dye labeling, without further signal amplification (Figure 1D-G).
372 *In vivo* 2-photon (2P) imaging of YFPpost-transduced dendrites from L2 Pyr neurons in mouse
373 S1 revealed that punctate YFP signal was associated with both dendritic shafts and spines (Figure
374 1H-J). Because FAPpost fluorescence required the addition of MG fluorogen, and *in vivo* imaging
375 was carried out using a cranial window with a glass coverslip after several days of recovery, it was
376 not straightforward to image FAPpost expression *in vivo*. Our results indicate that YFPpost is bright
377 enough for detection of puncta in living tissue. Overall, we find that NL-1 tethered fluorophores can
378 be detected in both fixed and living brain tissue without signal amplification, with punctate
379 expression that localizes to sites of synaptic input.

380 **Synapse localization without functional disruption**

381 Overexpression of other genetically-encoded synaptic proteins has been associated with
382 elevated synapse density and abnormal electrophysiological properties. For example, increased
383 anatomical synapse density and mEPSC frequency has been observed with overexpression of GFP-
384 tagged PSD-95, gephyrin, or intact NL-1 (Chubykin et al., 2005; El-Husseini et al., 2000; Gross et
385 al., 2013; Prange et al., 2004). Trans-synaptic interactions for split protein indicators have been
386 shown to increase binding affinities for the tagged proteins, and irreversible GFP-reconstitution can
387 perturb synapse stability and organization (Tsetsenis et al., 2014; Yamagata and Sanes, 2012).
388 Electrophysiological recordings can be a sensitive way to survey alterations in synaptic
389 function, independent of anatomical quantitation from fluorescence images. To test whether FAPpost
390 expression was associated with altered mEPSC and mIPSC properties, adjacent untransfected and
391 dTom+, FAPpost transfected cells were targeted for whole-cell recordings (Figure 2).

392 FAPpost expression did not alter mean mEPSC frequency or amplitude (Figure 2B; frequency
393 untransfected 2.3±0.5 Hz vs FAPpost 1.9±0.4 Hz; amplitude untransfected 12.5±1.0 pA versus
394 FAPpost 12.8±0.7 pA). Furthermore, mean mIPSC frequency and amplitude were not significantly
395 different (Figure 2E; frequency untransfected 1.8±0.5 Hz versus FAPpost 2.3±0.4 Hz; amplitude
396 untransfected 11.5±0.9 pA vs FAPpost 10.8±0.6 pA), although a small reduction in the frequency
397 distribution of mIPSCs was observed (Figure 2F). Thus, expression of postsynaptic fluorophores
398 using NL-1 targeting sequences can be a non-invasive way to identify and quantitate synaptic
399 distributions without altering synaptic function.

400 To test whether FAPpost synaptic labeling was detecting inhibitory synaptic contacts onto a
401 cell, we evaluated the alignment of FAPpost signal with immunohistochemical detection of a
402 ubiquitous presynaptic marker, bassoon (Richter et al., 1999). We focused on FAPpost labeling at the
403 soma, since synapses here were easily detected in confocal cross-sections. Bassoon
404 immunohistochemistry was carried out in PV-Cre x Ai3 tissue (where PV neurites were labeled with
405 YFP), and bassoon alignment to FAPpost-expressing Pyr neurons in L2 was assessed (Figure 3A-E).
406 More than 90% of bassoon puncta aligned with FAPpost puncta (Figure 3F), where only 7±10%
407 (mean±SD) of bassoon+ PV lacked FAPpost signal. In 3/5 cells analyzed, we observed that all PV
408 terminals showed both bassoon and FAPpost. This suggests that FAPpost labels that vast majority of
409 synaptic contacts from PV neurons. FAPpost puncta showed a slightly lower rate of alignment with
410 presynaptic bassoon (84±10% of detected FAPpost puncta could be aligned to a bassoon puncta;
411 Figure 3G). For FAPpost puncta that did not show bassoon labeling, 12±6% were aligned to PV
412 terminals – and were thus likely to be bona fide synaptic contacts. We attribute FAPpost and PV-
413 aligned but bassoon immunonegative terminals to either true bassoon-negative release sites
414 (Dondzillo et al., 2010) or incomplete labeling with the bassoon antibody, either from poor antibody
415 penetration or due to small bassoon puncta that were not detectable given our labeling and imaging
416 conditions. More than 70% of identified PV terminals also showed FAPpost expression (Figure 3H).

17

417 It is likely that some putative PV terminals apposed to the soma were not actual release sites, since
418 the overwhelming majority (95%) of PV+ terminals aligned with FAPpost also showed presynaptic
419 bassoon signal.

420 Since our analysis focused on PV inputs at the soma, these data provide evidence that FAPpost
421 effectively labels at least one class of inhibitory synapses. Because we did not evaluate the presence
422 of FAPpost at all synapse types defined by distinct pre- and postsynaptic cell types, we cannot be
423 assured that it is equally distributed for all potential synaptic contacts.

424 We also carried out bassoon immuno-colocalization for FAPpost puncta along spiny dendrites
425 from putative Pyr neurons. Analysis of 11 dendritic segments showed that >90% of FAPpost puncta
426 were associated with bassoon (Figure 3I-M). Because synapses are densely distributed across a
427 volume of brain tissue, and there are many synapses near a labeled segment that belong to an
428 unlabeled pair of neurons, it was not possible to determine false negative rates (i.e. bassoon but not
429 FAPpost for a given dendritic segment). Some FAPpost puncta had no detectable bassoon associated
430 signal. This may result from either an inability to detect bassoon (low fluorescence signal or
431 subthreshold levels of bassoon) or from a bona fide false positive, perhaps due to FAPpost signal that
432 may not be synaptically localized.

433 **High-throughput synapse quantitation**

434 To facilitate high-throughput quantitative fluorescence analysis of synapses in neurons from
435 brain tissue, we applied an efficient and scalable analysis pipeline with automated synapse detection
436 and assignment. Sparse viral transduction of FAPpost in Pyr neurons from primary somatosensory
437 (barrel) cortex revealed Pyr neurons decorated with bright, FAP puncta across the cell surface (Figure
438 4A). Using Imaris image analysis software, neural surfaces were rendered and puncta assigned to an
439 individual neuron for quantitative analysis. Because dendritic spines were not always visible from the
440 dTom fill, FAPpost puncta that were 1µm from the parent dendrite were digitally assigned to a given

441 cell. This semi-automated approach enables high-throughput synapse identification and quantitative
442 analysis (4-1, 4-2 and Figure 4D-G).
443 Reconstructions of fixed specimens yielded 200-1000 µm of continuous dendritic segment per
444 neuron for analysis. Overall, FAPpost puncta densities across L2 Pyr dendrites, 2.3±0.1 puncta/µm
445 (excluding the 1° apical dendrite; see Methods) were similar to previous estimates of synapse density
446 (Gulyas et al., 1999; Hersch and White, 1981; Holtmaat et al., 2005; Kasthuri et al., 2015; Villa et al.,
447 2016a), supporting this high-throughput analytical approach. We also examined puncta densities in
448 L2 Pyr neurons from the Emx1-Cre transgenic mouse strain using a Cre-dependent YFPpost
449 construct (Figure 4-2). On average, puncta densities were elevated for L2 Pyr neurons in this strain
450 (2.9±0.1 puncta/µm), consistent with the elevated spontaneous activity and enhanced seizure
451 susceptibility that has been observed in this strain (Kim et al., 2013; Steinmetz et al., 2017).
452 We observed substantial heterogeneity in detected puncta density across individual L2 Pyr
453 neurons, with close to four-fold variance across cells (1.0-3.8 puncta/µm), and nearly 10-fold
454 variance (0.7 to 5.9 puncta/µm) across different dendritic branches (Figure 4G). We found no
455 relationship between mean puncta density and total dendritic length analyzed for a given neuron.
456 Variability in overall puncta density for any cell type could not generally be explained by sex, age,
457 days post-infection, or animal-to-animal differences as neurons with a range of puncta densities could
458 be found in the same animal (Table 1). It is likely that the number of viral particles infecting
459 individual neurons was not uniform, even in cells analyzed from the same animal, and may be an
460 additional source of heterogeneity in analysis of puncta densities; however, we found no significant
461 relationship between puncta intensity and puncta density across analyzed neurons. Dendritic puncta
462 density for a given cell was correlated with the soma density (R^2=0.37). Variability in observed
463 puncta density for Pyr neurons is consistent with anatomical and electrophysiological response
464 variability that has been described for this group of (Pronneke et al., 2015; Tasic et al., 2016; Tyler et

19

465 al., 2015; van Aerde and Feldmeyer, 2015; Yamashita et al., 2013; Yassin et al., 2010), and may
466 reflect both developmental and molecular heterogeneity of neocortical Pyr neurons.
467 Although we did not systematically evaluate FAPpost properties in inhibitory neurons, we
468 observed punctate fluorescence in PV, SST, and VIP neurons that expressed this postsynaptic label.
469 Thus, this tool may be useful for quantitative synapse analysis in multiple cell types.
470 Quantitative analysis across different dendritic compartments revealed that the primary (1°)
471 apical dendrite, a short region of dendrite that emerges from the soma of Pyr neurons, showed dense
472 FAPpost puncta (Figure 4I). The high density of putative synapses in this compartment has not been
473 well-described, in part because prior analyses have typically used dendritic spines as a proxy for
474 synapses and this region is characteristically smooth. Mean puncta density on higher-order dendritic
475 branches was similar across segments.

476 **Presynaptic input assignment using fluorescence-based colocalization**

477 Transsynaptic molecular complementation for synapse detection requires both pre- and
478 postsynaptic transgene expression and may introduce unwanted effects on synapse function. In
479 addition, because presynaptic input labels are not typically saturated using virally-introduced
480 transgenes, complete and quantitative comparisons of input densities across cells and conditions are
481 difficult. Here we assessed whether dendritic FAPpost could be used for identification of putative
482 synaptic contacts where presynaptic neurites are fully labeled using Cre-dependent YFP expression
483 in transgenic mice (Hippenmeyer et al., 2005; Taniguchi et al., 2011). The far-red emission of MG-
484 binding FAPs can be easily multiplexed with other commonly-used fluorophores for detection of
485 adjacent pre- and postsynaptic signals. Although many other studies have used the convergence of
486 pre-and postsynaptic histochemical or fluorescence signal (Kubota et al., 2015; Schoonover et al.,
487 2014) the introduction of a third feature that marks putative synapse location should improve the
488 accuracy of input-specific synapse assignment in genetically-selectable, sparsely-labeled target cells.

489 Initially we focused on the primary apical dendrite of L2 Pyr neurons, where FAPpost puncta
490 were clearly demarcated and densely distributed. Manual inspection of a confocal image series shows
491 YFP-labeled PV neurites associated with the dendrite in close proximity to FAPpost puncta (Figure
492 5A). Digital analysis of this 3-dimensional segment for both puncta detection and neurite surface
493 rendering enables a distance-based criterion for assigning specific puncta to PV inputs (Figure 5B-E).
494 A limitation of this fluorescence-based approach – for both us and in previous studies – is that
495 diffraction–limited images cannot perfectly differentiate between apparent and true synaptic contacts.
496 However, use of consistent analysis parameters across specimens may be sufficient to detect
497 condition-specific changes in input organization.

498 How does inclusion of synaptic marker improve the detection of putative synapses? We
499 compared the number of detected contacts using only fluorescence labeling of presynaptic neurites
500 and the postsynaptic cell, or using these two features plus the presence of a FAPpost puncta at a
501 contact site. We hypothesized that the number of putative synaptic contacts would be reduced when
502 a third feature was required for synapse detection, and thus this method might offer improvements
503 upon prior quantitative approaches. Analysis focused on YFP-labeled inputs to Pyr soma, where data
504 from prior EM and light-microscopy analyses could confirm our analysis (Di Cristo et al., 2004; Hill
505 et al., 2012; Kubota et al., 2016; Kubota et al., 2015; Melchitzky and Lewis, 2008; Tamas et al.,
506 2000; Zhou et al., 2017).

507 Using only neurite-associations with the postsynaptic soma – a method that has been frequently
508 used to estimate PV cell innervation (see for example (Di Cristo et al., 2004; Feldmeyer et al., 2006;
509 Hill et al., 2012)) – we estimated the number of putative somatic synapses for individual Pyr neurons.
510 We then compared these values for the same cell with additional requirement of a FAPpost puncta in
511 between the neurite and the postsynaptic soma, using a neurite-to-puncta distance detection threshold
512 of 0.15µm (Figure 6). The use of three features (presynaptic neurite, postsynaptic puncta, and
513 postsynaptic neuron) to quantify input density reduced the number of putative contacts, or false

21

514 positives, that likely result from non-synaptic neurite juxtaposition. In addition, we sometimes
515 observed neurite apposition at the soma that was associated with multiple underlying FAPpost
516 puncta, suggesting that prior methods using only pre- and postsynaptic proximity might have
517 underestimated actual synapse number. Overall, this analysis enabled us to obtain quantitative
518 information about synapse number using fluorescence imaging data more accurately than would be
519 provided by only pre- and postsynaptic neurite apposition.

520 We used this quantitative data to compare the density of inhibitory inputs to the soma across
521 three classes of inhibitory neurons. FAPpost puncta at the soma were more than 4-fold more likely to
522 be aligned with PV than SST neurites (mean±SD, somatic PV-assigned puncta 66±30, n=9 Pyr
523 neurons; versus somatic SST-assigned puncta 15±8, n=9 Pyr neurons, Figure 6). Analysis of VIP-
524 associated inputs revealed a small number of colocalized post-synaptic puncta at the soma (somatic
525 VIP-assigned puncta 11±16, <5% of total somatic puncta; n=9 Pyr neurons). Taken together,
526 approximately one-third of somatic puncta could be assigned to either PV, SST, or VIP inputs; the
527 stringency of our input-detection parameters likely underestimates the number of contacts,
528 particularly for PV neurons. Our findings are consistent with prior reports showing that the majority
529 of somatic inputs arise from PV neurons, with a minority of other inhibitory inputs (Di Cristo et al.,
530 2004; Hill et al., 2012; Kubota et al., 2016; Melchitzky and Lewis, 2008; Micheva and Beaulieu,
531 1995), and show that synapse identification improves the accuracy of quantitative input analysis.

532 **Somatic and dendritic inhibition is dominated by PV input**

533 It is commonly held that PV inputs preferentially target the soma and SST inputs, the dendrites
534 (particularly in L1; (Chen et al., 2015; Dienel and Lewis, 2018; Pi et al., 2013)). However,
535 quantitative evidence for this is lacking and indeed recent reports suggest that PV inputs may be
536 broadly arrayed across the dendritic arbor (Kubota et al., 2015). We compared the distribution of
537 PV, SST and VIP inputs across the soma and along Pyr dendrites, including 4° branches that could

538 extend >140µm from the soma center (Figure 7, with gallery of PV-assigned, SST-assigned, and
539 VIP-assigned inputs on individual L2 Pyr neurons in Figure 7-1, 7-2, and 7-3).
540 Because soma size could vary more than two-fold between neurons (complicating measures of
541 density), we compared the percent of total puncta that could be assigned to PV, SST, or VIP inputs
542 for individual Pyr soma. Somatic puncta were dominated by PV inputs, where on average 25% of
543 FAPpost puncta could be assigned to adjacent PV neurites but only 5% of FAPpost puncta could be
544 assigned to SST inputs. In general, VIP inputs were rarely observed on L2 Pyr soma (Figure 7C,F).
545 Quantitative input assignment revealed that PV inputs were frequently observed along all
546 dendrites where their distribution only modestly declined at higher branch orders (up to 4° branches;
547 Figure 7F,H). On average, dendritic SST inputs were less abundant than PV inputs, using either
548 density measurements (mean density dendritic SST-assigned puncta 0.20±0.03/µm versus PV-
549 assigned puncta 0.38±0.07/µm, excluding the 1° apical dendrite for both) or relative proportion of
550 assigned puncta (Figure 7G). Even in higher-order (3° and 4°) apical dendrites, SST inputs were not
551 more numerous than PV inputs (Figure 7H). It remains possible that the L1 apical tuft of L2 Pyr
552 neurons (that was not included in our analysis, due to sectioning artifacts) may contain dense SST
553 inputs. Overall, quantitative input analysis shows that both PV and SST inputs are broadly distributed
554 across the dendrites of Pyr neurons within L2/3.
555 Interestingly, we observed a pronounced concentration of PV inputs at the synapse-dense 1°
556 apical dendrite as it emerged from the soma in L2 Pyr neurons (Figure 7A,B,H), with a significant 6-
557 fold greater density than for SST inputs. These data suggest that the 1° apical compartment might be
558 an extension of the soma with respect to PV presynaptic targeting and synaptic integration properties.
559 The prominent absence of SST inputs at the somatic and 1° apical dendrite suggests that SST neurons
560 may selectively avoid these PV-input-enriched perisomatic compartments (Figure 7G, H). Cortical
561 wiring diagrams showing SST input are frequently schematized to indicate the apical dendrite or L1
562 as the primary site of synaptic input (Chen et al., 2015; Dienel and Lewis, 2018; Pi et al., 2013). Our

23

data indicate that SST inputs are detectable across the dendritic arbor and may not be restricted to this layer.

VIP inputs to Pyr neurons showed a slightly higher density for the 1° apical versus other dendrites, although the absolute number of synapses was very low. Overall, VIP input density was 10-fold lower than PV inputs to the 1° apical dendrite, a difference that was highly significant (Figure 7G). For higher-order dendrites, VIP input density was significantly lower than either PV and SST inputs (mean density, dendritic VIP-assigned puncta excluding the 1° apical dendrite 0.07±0.01/µm). These differences were also reflected in the relative proportion, in addition to the density, of assigned FAPpost puncta. For example, at higher-order apical dendrites the proportion of total SST-assigned puncta (10.5±1.9% of total inputs) was slightly lower than the proportion of PV-assigned puncta (16.2±1.9% of total inputs), but significantly greater than VIP inputs (1.4±1.9%).

Because there are a small fraction of PV-Cre expressing Pyr neurons in deep layers, it is possible that some of the detected PV inputs may arise from PV-expressing Pyr neurons. However, PV-expressing Pyr neurons are not observed in L2, and it is likely that the majority of PV inputs arise from intralaminar inputs (Fino and Yuste, 2011). These findings are consistent with meticulous neuroanatomical reconstructions of synaptically-connected pairs showing that PV synapses can be observed across the dendritic arbor of neocortical Pyr neurons (Kubota et al., 2015). In addition, our data indicate that SST inputs are common across the dendritic arbor within L2. These data suggest revisions to previous cortical wiring diagrams that show SST inputs exclusively at the apical tuft and PV inputs exclusively at the soma (Chen et al., 2015; Dienel and Lewis, 2018; Pi et al., 2013).

Discussion

Synapses are a critical determinant of neural function, and their individual and collective properties can provide insight into how brain circuits are organized and changed by experience. Electrophysiological measurements of mEPSC and mIPSCs have been widely used to assess circuit-

level adaptations in synaptic function, but typically sample only a small subset of inputs onto a neuron close to the recording electrode due to electrical filtering of small and distant signals. In contrast, anatomical methods offer a highly quantitative, compartment-specific and anatomically broad view of how synapses and cell-type specific inputs are distributed onto a neuron.

A fluorescence-based, molecular genetic platform for synaptic detection and quantitation has multiple advantages for high-throughput and scalable analysis. First, the brightness of FAP/YFPpost synaptic tags enable direct visualization of synapses in both live and fixed tissue without amplification, making them accessible tools for broad scale use. Second, synaptically-targeted fluorophores can be sparsely expressed in brain tissue, not just cultured neurons, to reveal properties of synaptic and input organization in a complex neural circuit. Third, fluorescence imaging enables use of multiple, spectrally distinct channels for cell-type-selective identification of axonal inputs and specific molecules that can differentiate synapses. Fourth, volumetric data collection is rapid and requires only a confocal microscope, and images can be used for high-throughput, automated analysis. Overall, quantitative and high-throughput synapse detection with FAP/YFPpost will facilitate cell-type specific characterization of synapses and connectivity changes across multiple animals and diverse experimental conditions.

Synaptic quantitation without perturbation

Experimental evidence indicates that FAPpost labels both excitatory and inhibitory synapses. FAPpost puncta are localized to soma and dendritic shafts, preferred targets for inhibitory synapses as well as on dendritic spines where excitatory synapses lie. FAPpost convergence with presynaptic inputs from confirmed GABAergic neuron subtypes, specifically PV, SST, and VIP neurons, indicates association with inhibitory inputs. The FAPpost labeling of both excitatory and inhibitory synapses allows comprehensive analysis of synapse distribution from a single postsynaptic marker. Reagents that separately enable visualization of excitatory and inhibitory synapses will also be useful

25

612 tools for fluorescence-based quantitative imaging (Chen et al., 2015; Gross et al., 2013), if expression
613 levels are high enough for reliable synapse detection.

614 Although it has been proposed that NL-1 is specifically targeted to excitatory synapses (Song et
615 al., 1999), NL-1 contains a conserved binding motif for the GABAergic receptor scaffolding
616 molecule gephyrin and NL-1-based synapse labeling constructs are sometimes observed at inhibitory
617 synapses (Bemben et al., 2015; Kwon et al., 2018; Tsetsenis et al., 2014). Neurexin 1β-binding to the
618 extracellular portion of NL-1 has been shown to enhance intracellular PSD-95 interactions (Giannone
619 et al., 2013) and this region's deletion in FAPpost may enable the broader distribution observed in
620 transduced neurons. Importantly, prior studies have shown that the absence of the extracellular NL-1
621 region inhibits ectopic synapse formation (Chih et al., 2005), supporting the use of FAPpost as a non-
622 invasive tag for synapse monitoring.

623 Does FAPpost expression alter synaptic function *in vivo*? This is a significant issue, as the
624 electrophysiological effects of other fluorescence synapse detection reagents have not been well-
625 investigated (Choi et al., 2018; Kim et al., 2011; Martell et al., 2016). Overexpression of tagged
626 synaptic molecules leads to an increase in overall synapse number, using electrophysiological or
627 anatomical measurements (El-Husseini et al., 2000; Gross et al., 2013). In such cases, quantitative
628 analysis can be misleading, reflecting either a primary overexpression effect or a secondary effect of
629 circuit-level adjustments to abnormal synaptic input. The absence of a clear electrophysiological
630 phenotype for the FAPpost reagent suggests that overexpression of our fluorophore-tagged NL-1, in
631 the absence of trans-synaptic interactions, may have a minimal effect on synaptic function.

632 **Synapse detection accuracy**

633 How does FAPpost synaptic quantitation compare to previous estimates of synaptic density and
634 input organization? Synapse density has often been estimated indirectly from fluorescence images,
635 using spines as a proxy for synapses. This is problematic, as spine detection will underestimate
636 synapse number by excluding shaft synapses (typically inhibitory), dually-innervated spines (>10%

637 by some estimates (Chen et al., 2012), spines that lie within the imaging plane, and will also
638 undercount faintly labeled, filamentous spines.

639 Overall synapse densities for L2 Pyr neurons revealed an overall average of 2.8 synapses/µm
640 dendrite, a density that is well within the range of prior estimates. For example, whole-cell EM
641 reconstructions of CA1 hippocampal neurons have shown synapse densities of 0.7-7 synapses/µm,
642 depending on location within the dendrite (Gulyas et al., 1999). Other studies analyzing spine (not
643 synapse) density from L2 or L5 Pyr neurons in mouse S1 report between 0.4-5.1 spines/µm, where
644 EM studies typically reveal greater spine densities (Holtmaat et al., 2005; Kasthuri et al., 2015; Villa
645 et al., 2016a).

646 Fluorescence-based synaptic tags reduce multiple sources of error that can inaccurately assess
647 total synapse number. For isolated neurons, automated puncta assignment to the parent dendrite
648 removes the requirement that dendritic spines be visible for synapse detection, reducing false-
649 negative rates. For automated assignment, this rate will always be non-zero as the distance limit set
650 for puncta assignment will exclude puncta that lie on longer dendritic spines, which can extend >5µm
651 in some cases (Kasthuri et al., 2015).

652 False-positive (non-synaptic puncta) errors are more difficult to estimate. Intracellular pools of
653 the targeting construct may contribute. Although these were digitally excluded based upon distance
654 to the plasma membrane, this process that may not be effective for thin dendritic segments. It is
655 possible that non-synaptic, plasma-membrane FAPpost accumulation may sometimes occur. In
656 addition, puncta from nearby neurons may have been inadvertently misassigned to an analyzed
657 dendritic segment. While fluorescence-based genetic methods have advantages, they are subject to
658 variations in expression levels, both of the labeling construct and of protein trafficking to different
659 synapses (for example, that may have a lower NL-1 content or are more distant from the soma). It
660 remains possible that not all synapses – for example, neuromodulatory or peptidergic inputs – were
661 uniformly labeled using this methodology. The quantitative analysis pipeline established here

27

662 attempts to reconcile high-throughput analysis with variability in synapse structure, where speed and
663 accuracy must be balanced.

664 **Biological and non-biological variability**

665 We observed marked within (10-20-fold) and across cell (2-4-fold) variability in FAP/YFPpost
666 synapse density within and across L2 Pyr neurons. Variability in synapse density and its biological
667 implications has not been well-explored. Most analyses have focused on complete reconstruction of a
668 single neuron (Megías et al., 2001) or of a few dendritic segments (Kasthuri et al., 2015; Villa et al.,
669 2016 and others). In one study that carried out a detailed analysis of multiple pyramidal cells' apical
670 dendrites, a wide range of synapse densities were observed (Hersch and White, 1981). Cells with
671 higher synapse densities may represent "hub" cells that receive wide distribution of synaptic inputs,
672 or more recurrent connections from the same presynaptic neuron(s). Notably, miniature postsynaptic
673 current frequency data (both ours and others) shows a 10-fold range in values across pyramidal
674 neurons. Mini frequencies are typically interpreted as reflecting the number of synaptic connection
675 on a given postsynaptic cell. Considering the electrophysiological correlate of synapse number shows
676 a similar range in values to anatomical correlates of synapses on pyramidal neurons, we may very
677 well be capturing normal biological variability in synapse numbers.

678 Alternatively, observed variability may be a non-biological labeling artefact. To achieve
679 complete synaptic labeling, expression of any synapse-tagging molecule must reach sufficient levels
680 in an individual cell to label all synapses across its entire dendritic arbor. It is unlikely that this
681 labeling occurs at the same time for all cells. One alternative explanation for the wide-range in
682 synapse densities is that only a fraction of synapses were labeled in a particular cell. We attempted to
683 control for this by only selecting well-labeled cells, but we cannot rule out this potential confound in
684 the interpretation of our findings.

685 **Volumetric imaging for high-throughput synaptic input assignment**

686 A significant advance enabled by an all-fluorescence synaptic imaging platform is the
687 automated assignment of cell-type specific synaptic inputs with a spectrally distinct fluorophore. The
688 tricolor (FAPpost, dTom, and presynaptic YFP) association as a criterion for synapse detection
689 substantially reduces the false positive rate compared to brightfield microscopy methods (Hill et al.,
690 2012; Kubota et al., 2015; Schoonover et al., 2014). We took advantage of the complete labeling of
691 molecularly-defined inhibitory neuron populations in Cre-driver transgenic mouse lines to examine
692 the broad-scale distribution of FAPpost labeled synaptic inputs on L2 Pyr neurons that originated
693 from three types of GABAergic neurons.

694 Our analysis revealed that PV inputs predominate at somatic locations, with approximately six
695 times as many PV as SST inputs to the cell body. These data are consistent with reports of dense PV
696 innervation of the soma (Kubota et al., 2016) and a small fraction of somatic SST inputs (<10%)
697 (Hill et al., 2012), and further validate FAPpost labeling as a robust method for quantitative synapse
698 assignment. Dendritic analysis of synapse organization identified the 1° apical dendrite of Pyr
699 neurons as a site of particularly dense PV innervation. This aspiny region of the dendrite,
700 particularly in neocortical Pyr neurons, has been poorly studied as prior imaging methods have not
701 been able to reliably visualize synapses in this compartment. Importantly, whole-neuron EM
702 reconstructions show that >90% of inputs to the apical dendrite of CA1 neurons are inhibitory (Bloss
703 et al., 2016; Megias et al., 2001). The distinctive properties of the apical dendrite (Major et al., 2013)
704 suggest that PV input to this region may serve as a critical filter for top-down modulation of Pyr
705 neuron firing in the neocortex.

706 Quantitative analysis showed that PV neurons have more input to Pyr neuron dendrites than
707 other neocortical inhibitory neurons. Indeed, even when excluding the densely PV-innervated 1°
708 apical dendrite, mean dendritic input density was greater for PV than SST, and VIP inputs. Although
709 this may be incongruous with the simplified model that contrasts soma-targeting PV and dendrite-
710 targeting SST inputs (Chen et al., 2015; Higley, 2014; Lazarus and Huang, 2011; Pakan et al., 2016;

29

Pi et al., 2013), prior experimental data are much less categorical than these schema suggest. For example, anatomical reconstructions from paired whole-cell recordings show that the majority of PV inputs to neocortical pyramidal neurons are located >50µm from the soma (Hill et al., 2012; Kubota et al., 2015) and abundant SST contacts can be detected at both proximal and distal dendrites (Di Cristo et al., 2004; Hill et al., 2012). It remains possible that very distal dendrites, particularly in L1, have a disproportionate association of SST inputs. Based on the density of synaptic inputs, our data indicate that PV-mediated synaptic input will be the predominant source of inhibition across the somatodendritic compartments of L2 Pyr neurons.

Conclusion

This analysis helps generate a framework for large-scale anatomical imaging to examine circuit- and brain-wide changes in synapse distribution in development, learning, and disease. Future efforts should leverage volumetric imaging in cleared or expanded tissue for complete and high-resolution capture of the entire dendritic apparatus, application of additional molecular markers to distinguish different synapse types, and will employ new presynaptic constructs for improved synaptic discrimination. A critical challenge of these future possibilities will be the digital capture and storage of large anatomical datasets for computational analysis.

727 **References**

728 Bayes, A., van de Lagemaat, L.N., Collins, M.O., Croning, M.D., Whittle, I.R., Choudhary, J.S., and
729 Grant, S.G. (2011). Characterization of the proteome, diseases and evolution of the human
730 postsynaptic density. Nature neuroscience *14*, 19-21.

731 Bemben, M.A., Shipman, S.L., Nicoll, R.A., and Roche, K.W. (2015). The cellular and molecular
732 landscape of neuroligins. Trends Neurosci *38*, 496-505.

733 Bloss, E.B., Cembrowski, M.S., Karsh, B., Colonell, J., Fetter, R.D., and Spruston, N. (2016).
734 Structured Dendritic Inhibition Supports Branch-Selective Integration in CA1 Pyramidal Cells.
735 Neuron *89*, 1016-1030.

736 Bock, D.D., Lee, W.C., Kerlin, A.M., Andermann, M.L., Hood, G., Wetzel, A.W., Yurgenson, S.,
737 Soucy, E.R., Kim, H.S., and Reid, R.C. (2011). Network anatomy and in vivo physiology of
738 visual cortical neurons. Nature *471*, 177-182.

739 Briggman, K.L., Helmstaedter, M., and Denk, W. (2011). Wiring specificity in the direction-selectivity
740 circuit of the retina. Nature *471*, 183-188.

741 Chandrasekaran, S., Navlakha, S., Audette, N.J., McCreary, D.D., Suhan, J., Bar-Joseph, Z., and Barth,
742 A.L. (2015). Unbiased, High-Throughput Electron Microscopy Analysis of Experience-
743 Dependent Synaptic Changes in the Neocortex. J Neurosci *35*, 16450-16462.

744 Chen, J.L., Villa, K.L., Cha, J.W., So, P.T., Kubota, Y., and Nedivi, E. (2012). Clustered dynamics of
745 inhibitory synapses and dendritic spines in the adult neocortex. Neuron *74*, 361-373.

746 Chen, S.X., Kim, A.N., Peters, A.J., and Komiyama, T. (2015). Subtype-specific plasticity of
747 inhibitory circuits in motor cortex during motor learning. Nature neuroscience *18*, 1109-1115.

748 Chih, B., Engelman, H., and Scheiffele, P. (2005). Control of excitatory and inhibitory synapse
749 formation by neuroligins. Science *307*, 1324-1328.

31

750 Choi, J.H., Sim, S.E., Kim, J.I., Choi, D.I., Oh, J., Ye, S., Lee, J., Kim, T., Ko, H.G., Lim, C.S., *et al.*
751 (2018). Interregional synaptic maps among engram cells underlie memory formation. Science
752 *360*, 430-435.
753 Chubykin, A.A., Liu, X., Comoletti, D., Tsigelny, I., Taylor, P., and Sudhof, T.C. (2005). Dissection of
754 synapse induction by neuroligins: effect of a neuroligin mutation associated with autism. J Biol
755 Chem *280*, 22365-22374.
756 Di Cristo, G., Wu, C., Chattopadhyaya, B., Ango, F., Knott, G., Welker, E., Svoboda, K., and Huang,
757 Z.J. (2004). Subcellular domain-restricted GABAergic innervation in primary visual cortex in the
758 absence of sensory and thalamic inputs. Nature neuroscience *7*, 1184-1186.
759 Dienel, S.J., and Lewis, D.A. (2018). Alterations in cortical interneurons and cognitive function in
760 schizophrenia. Neurobiol Dis.
761 Dondzillo, A., Satzler, K., Horstmann, H., Altrock, W.D., Gundelfinger, E.D., and Kuner, T. (2010).
762 Targeted three-dimensional immunohistochemistry reveals localization of presynaptic proteins
763 Bassoon and Piccolo in the rat calyx of Held before and after the onset of hearing. J Comp Neurol
764 *518*, 1008-1029.
765 Druckmann, S., Feng, L., Lee, B., Yook, C., Zhao, T., Magee, J.C., and Kim, J. (2014). Structured
766 synaptic connectivity between hippocampal regions. Neuron *81*, 629-640.
767 El-Husseini, A.E., Schnell, E., Chetkovich, D.M., Nicoll, R.A., and Bredt, D.S. (2000). PSD-95
768 involvement in maturation of excitatory synapses. Science *290*, 1364-1368.
769 Feldmeyer, D., Lubke, J., and Sakmann, B. (2006). Efficacy and connectivity of intracolumnar pairs of
770 layer 2/3 pyramidal cells in the barrel cortex of juvenile rats. The Journal of physiology *575*, 583-
771 602.
772 Fino, E., and Yuste, R. (2011). Dense inhibitory connectivity in neocortex. Neuron *69*, 1188-1203.

773 Fortin, D.A., Tillo, S.E., Yang, G., Rah, J.C., Melander, J.B., Bai, S., Soler-Cedeno, O., Qin, M.,
774 Zemelman, B.V., Guo, C., *et al.* (2014). Live imaging of endogenous PSD-95 using ENABLED:
775 a conditional strategy to fluorescently label endogenous proteins. J Neurosci *34*, 16698-16712.
776 Giannone, G., Mondin, M., Grillo-Bosch, D., Tessier, B., Saint-Michel, E., Czondor, K., Sainlos, M.,
777 Choquet, D., and Thoumine, O. (2013). Neurexin-1beta binding to neuroligin-1 triggers the
778 preferential recruitment of PSD-95 versus gephyrin through tyrosine phosphorylation of
779 neuroligin-1. Cell Rep *3*, 1996-2007.
780 Glausier, J.R., Roberts, R.C., and Lewis, D.A. (2017). Ultrastructural analysis of parvalbumin synapses
781 in human dorsolateral prefrontal cortex. J Comp Neurol *525*, 2075-2089.
782 Gross, G.G., Junge, J.A., Mora, R.J., Kwon, H.B., Olson, C.A., Takahashi, T.T., Liman, E.R., Ellis-
783 Davies, G.C., McGee, A.W., Sabatini, B.L., *et al.* (2013). Recombinant probes for visualizing
784 endogenous synaptic proteins in living neurons. Neuron *78*, 971-985.
785 Gulyas, A.I., Megias, M., Emri, Z., and Freund, T.F. (1999). Total number and ratio of excitatory and
786 inhibitory synapses converging onto single interneurons of different types in the CA1 area of the
787 rat hippocampus. J Neurosci *19*, 10082-10097.
788 Hersch, S.M., and White, E.L. (1981). Quantification of synapses formed with apical dendrites of
789 Golgi-impregnated pyramidal cells: variability in thalamocortical inputs, but consistency in the
790 ratios of asymmetrical to symmetrical synapses. Neuroscience *6*, 1043-1051.
791 Higley, M.J. (2014). Localized GABAergic inhibition of dendritic Ca(2+) signalling. Nat Rev Neurosci
792 *15*, 567-572.
793 Hill, S.L., Wang, Y., Riachi, I., Schurmann, F., and Markram, H. (2012). Statistical connectivity
794 provides a sufficient foundation for specific functional connectivity in neocortical neural
795 microcircuits. Proc Natl Acad Sci U S A *109*, E2885-2894.

33

796 Hippenmeyer, S., Vrieseling, E., Sigrist, M., Portmann, T., Laengle, C., Ladle, D.R., and Arber, S.
797 (2005). A developmental switch in the response of DRG neurons to ETS transcription factor
798 signaling. PLoS Biol *3*, e159.
799 Holtmaat, A.J., Trachtenberg, J.T., Wilbrecht, L., Shepherd, G.M., Zhang, X., Knott, G.W., and
800 Svoboda, K. (2005). Transient and persistent dendritic spines in the neocortex in vivo. Neuron
801 *45*, 279-291.
802 Kasthuri, N., Hayworth, K.J., Berger, D.R., Schalek, R.L., Conchello, J.A., Knowles-Barley, S., Lee,
803 D., Vazquez-Reina, A., Kaynig, V., Jones, T.R.*, et al.* (2015). Saturated Reconstruction of a
804 Volume of Neocortex. Cell *162*, 648-661.
805 Kim, J., Zhao, T., Petralia, R.S., Yu, Y., Peng, H., Myers, E., and Magee, J.C. (2011). mGRASP
806 enables mapping mammalian synaptic connectivity with light microscopy. Nat Methods *9*, 96-
807 102.
808 Kim, J.S., Greene, M.J., Zlateski, A., Lee, K., Richardson, M., Turaga, S.C., Purcaro, M., Balkam, M.,
809 Robinson, A., Behabadi, B.F.*, et al.* (2014). Space-time wiring specificity supports direction
810 selectivity in the retina. Nature *509*, 331-336.
811 Kim, T.H., Richards, K., Heng, J., Petrou, S., and Reid, C.A. (2013). Two lines of transgenic mice
812 expressing cre-recombinase exhibit increased seizure susceptibility. Epilepsy Res *104*, 11-16.
813 Kinoshita, N., Huang, A.J.Y., McHugh, T.J., Suzuki, S.C., Masai, I., Kim, I.H., Soderling, S.H.,
814 Miyawaki, A., and Shimogori, T. (2019). Genetically Encoded Fluorescent Indicator GRAPHIC
815 Delineates Intercellular Connections. iScience *15*, 28-38.
816 Kornfeld, J., Benezra, S.E., Narayanan, R.T., Svara, F., Egger, R., Oberlaender, M., Denk, W., and
817 Long, M.A. (2017). EM connectomics reveals axonal target variation in a sequence-generating
818 network. Elife *6*.

819 Kremers, G.J., Goedhart, J., van Munster, E.B., and Gadella, T.W., Jr. (2006). Cyan and yellow super
820 fluorescent proteins with improved brightness, protein folding, and FRET Forster radius.
821 Biochemistry *45*, 6570-6580.
822 Kubota, Y., Karube, F., Nomura, M., and Kawaguchi, Y. (2016). The Diversity of Cortical Inhibitory
823 Synapses. Front Neural Circuits *10*, 27.
824 Kubota, Y., Kondo, S., Nomura, M., Hatada, S., Yamaguchi, N., Mohamed, A.A., Karube, F., Lubke,
825 J., and Kawaguchi, Y. (2015). Functional effects of distinct innervation styles of pyramidal cells
826 by fast spiking cortical interneurons. Elife *4*.
827 Kwon, O., Feng, L., Druckmann, S., and Kim, J. (2018). Schaffer Collateral Inputs to CA1 Excitatory
828 and Inhibitory Neurons Follow Different Connectivity Rules. J Neurosci *38*, 5140-5152.
829 Lazarus, M.S., and Huang, Z.J. (2011). Distinct maturation profiles of perisomatic and dendritic
830 targeting GABAergic interneurons in the mouse primary visual cortex during the critical period
831 of ocular dominance plasticity. Journal of neurophysiology *106*, 775-787.
832 Major, G., Larkum, M.E., and Schiller, J. (2013). Active properties of neocortical pyramidal neuron
833 dendrites. Annu Rev Neurosci *36*, 1-24.
834 Martell, J.D., Yamagata, M., Deerinck, T.J., Phan, S., Kwa, C.G., Ellisman, M.H., Sanes, J.R., and
835 Ting, A.Y. (2016). A split horseradish peroxidase for the detection of intercellular protein-protein
836 interactions and sensitive visualization of synapses. Nat Biotechnol *34*, 774-780.
837 Megias, M., Emri, Z., Freund, T.F., and Gulyas, A.I. (2001). Total number and distribution of
838 inhibitory and excitatory synapses on hippocampal CA1 pyramidal cells. Neuroscience *102*, 527-
839 540.
840 Melchitzky, D.S., and Lewis, D.A. (2008). Dendritic-targeting GABA neurons in monkey prefrontal
841 cortex: comparison of somatostatin- and calretinin-immunoreactive axon terminals. Synapse *62*,
842 456-465.

35

843 Micheva, K.D., and Beaulieu, C. (1995). An anatomical substrate for experience-dependent plasticity
844 of the rat barrel field cortex. Proc Natl Acad Sci U S A *92*, 11834-11838.
845 Micheva, K.D., and Smith, S.J. (2007). Array tomography: a new tool for imaging the molecular
846 architecture and ultrastructure of neural circuits. Neuron *55*, 25-36.
847 Pakan, J.M., Lowe, S.C., Dylda, E., Keemink, S.W., Currie, S.P., Coutts, C.A., and Rochefort, N.L.
848 (2016). Behavioral-state modulation of inhibition is context-dependent and cell type specific in
849 mouse visual cortex. Elife *5*.
850 Pi, H.J., Hangya, B., Kvitsiani, D., Sanders, J.I., Huang, Z.J., and Kepecs, A. (2013). Cortical
851 interneurons that specialize in disinhibitory control. Nature *503*, 521-524.
852 Prange, O., Wong, T.P., Gerrow, K., Wang, Y.T., and El-Husseini, A. (2004). A balance between
853 excitatory and inhibitory synapses is controlled by PSD-95 and neuroligin. Proc Natl Acad Sci U
854 S A *101*, 13915-13920.
855 Pratt, C.P., Kuljis, D.A., Homanics, G.E., He, J., Kolodieznyi, D., Dudem, S., Hollywood, M.A., Barth,
856 A.L., and Bruchez, M.P. (2017). Tagging of Endogenous BK Channels with a Fluorogen-
857 Activating Peptide Reveals beta4-Mediated Control of Channel Clustering in Cerebellum. Front
858 Cell Neurosci *11*, 337.
859 Pronneke, A., Scheuer, B., Wagener, R.J., Mock, M., Witte, M., and Staiger, J.F. (2015).
860 Characterizing VIP Neurons in the Barrel Cortex of VIPcre/tdTomato Mice Reveals Layer-
861 Specific Differences. Cereb Cortex *25*, 4854-4868.
862 Richter, K., Langnaese, K., Kreutz, M.R., Olias, G., Zhai, R., Scheich, H., Garner, C.C., and
863 Gundelfinger, E.D. (1999). Presynaptic cytomatrix protein bassoon is localized at both excitatory
864 and inhibitory synapses of rat brain. J Comp Neurol *408*, 437-448.
865 Scheiffele, P., Fan, J., Choih, J., Fetter, R., and Serafini, T. (2000). Neuroligin expressed in
866 nonneuronal cells triggers presynaptic development in contacting axons. Cell *101*, 657-669.

867 Schoonover, C.E., Tapia, J.C., Schilling, V.C., Wimmer, V., Blazeski, R., Zhang, W., Mason, C.A.,
868 and Bruno, R.M. (2014). Comparative strength and dendritic organization of thalamocortical and
869 corticocortical synapses onto excitatory layer 4 neurons. J Neurosci *34*, 6746-6758.
870 Song, J.Y., Ichtchenko, K., Sudhof, T.C., and Brose, N. (1999). Neuroligin 1 is a postsynaptic cell-
871 adhesion molecule of excitatory synapses. Proc Natl Acad Sci U S A *96*, 1100-1105.
872 Steinmetz, N.A., Buetfering, C., Lecoq, J., Lee, C.R., Peters, A.J., Jacobs, E.A.K., Coen, P.,
873 Ollerenshaw, D.R., Valley, M.T., de Vries, S.E.J.*, et al.* (2017). Aberrant Cortical Activity in
874 Multiple GCaMP6-Expressing Transgenic Mouse Lines. eNeuro *4*.
875 Sudhof, T.C. (2017). Synaptic Neurexin Complexes: A Molecular Code for the Logic of Neural
876 Circuits. Cell *171*, 745-769.
877 Szent-Gyorgyi, C., Schmidt, B.F., Creeger, Y., Fisher, G.W., Zakel, K.L., Adler, S., Fitzpatrick, J.A.,
878 Woolford, C.A., Yan, Q., Vasilev, K.V.*, et al.* (2008). Fluorogen-activating single-chain
879 antibodies for imaging cell surface proteins. Nat Biotechnol *26*, 235-240.
880 Szent-Gyorgyi, C., Stanfield, R.L., Andreko, S., Dempsey, A., Ahmed, M., Capek, S., Waggoner, A.S.,
881 Wilson, I.A., and Bruchez, M.P. (2013). Malachite green mediates homodimerization of antibody
882 VL domains to form a fluorescent ternary complex with singular symmetric interfaces. J Mol
883 Biol *425*, 4595-4613.
884 Tamas, G., Buhl, E.H., Lorincz, A., and Somogyi, P. (2000). Proximally targeted GABAergic synapses
885 and gap junctions synchronize cortical interneurons. Nature neuroscience *3*, 366-371.
886 Tang, A.H., Chen, H., Li, T.P., Metzbower, S.R., MacGillavry, H.D., and Blanpied, T.A. (2016). A
887 trans-synaptic nanocolumn aligns neurotransmitter release to receptors. Nature *536*, 210-214.
888 Taniguchi, H., He, M., Wu, P., Kim, S., Paik, R., Sugino, K., Kvitsiani, D., Fu, Y., Lu, J., Lin, Y.*, et al.*
889 (2011). A resource of Cre driver lines for genetic targeting of GABAergic neurons in cerebral
890 cortex. Neuron *71*, 995-1013.

37

891 Tasic, B., Menon, V., Nguyen, T.N., Kim, T.K., Jarsky, T., Yao, Z., Levi, B., Gray, L.T., Sorensen,
892 S.A., Dolbeare, T., *et al.* (2016). Adult mouse cortical cell taxonomy revealed by single cell
893 transcriptomics. Nature neuroscience *19*, 335-346.
894 Telmer, C.A., Verma, R., Teng, H., Andreko, S., Law, L., and Bruchez, M.P. (2015). Rapid, specific,
895 no-wash, far-red fluorogen activation in subcellular compartments by targeted fluorogen
896 activating proteins. ACS Chem Biol *10*, 1239-1246.
897 Tsetsenis, T., Boucard, A.A., Arac, D., Brunger, A.T., and Sudhof, T.C. (2014). Direct visualization of
898 trans-synaptic neurexin-neuroligin interactions during synapse formation. J Neurosci *34*, 15083-
899 15096.
900 Tyler, W.A., Medalla, M., Guillamon-Vivancos, T., Luebke, J.I., and Haydar, T.F. (2015). Neural
901 precursor lineages specify distinct neocortical pyramidal neuron types. J Neurosci *35*, 6142-6152.
902 van Aerde, K.I., and Feldmeyer, D. (2015). Morphological and physiological characterization of
903 pyramidal neuron subtypes in rat medial prefrontal cortex. Cereb Cortex *25*, 788-805.
904 Villa, K.L., Berry, K.P., Subramanian, J., Cha, J.W., Chan Oh, W., Kwon, H.B., Kubota, Y., So, P.T.,
905 and Nedivi, E. (2016a). Inhibitory Synapses Are Repeatedly Assembled and Removed at
906 Persistent Sites In Vivo. Neuron *90*, 662-664.
907 Villa, K.L., Berry, K.P., Subramanian, J., Cha, J.W., Oh, W.C., Kwon, H.B., Kubota, Y., So, P.T., and
908 Nedivi, E. (2016b). Inhibitory Synapses Are Repeatedly Assembled and Removed at Persistent
909 Sites In Vivo. Neuron *89*, 756-769.
910 Vishwanathan, A., Daie, K., Ramirez, A.D., Lichtman, J.W., Aksay, E.R.F., and Seung, H.S. (2017).
911 Electron Microscopic Reconstruction of Functionally Identified Cells in a Neural Integrator. Curr
912 Biol *27*, 2137-2147 e2133.
913 Yamagata, M., and Sanes, J.R. (2012). Transgenic strategy for identifying synaptic connections in mice
914 by fluorescence complementation (GRASP). Front Mol Neurosci *5*, 18.

915 Yamashita, T., Pala, A., Pedrido, L., Kremer, Y., Welker, E., and Petersen, C.C. (2013). Membrane
916 potential dynamics of neocortical projection neurons driving target-specific signals. Neuron *80*,
917 1477-1490.
918 Yassin, L., Benedetti, B.L., Jouhanneau, J.S., Wen, J.A., Poulet, J.F., and Barth, A.L. (2010). An
919 embedded subnetwork of highly active neurons in the neocortex. Neuron *68*, 1043-1050.
920 Zhou, X., Rickmann, M., Hafner, G., and Staiger, J.F. (2017). Subcellular Targeting of VIP Boutons in
921 Mouse Barrel Cortex is Layer-Dependent and not Restricted to Interneurons. Cereb Cortex *27*,
922 5353-5368.

39

Figure/Table/Extended Data Legends

Figure 1: Construct design and expression in mouse somatosensory (S1 barrelfield) cortex. (A) FAPpost and YFPpost construct design. Human synapsin promotor (hSyn) driving either a constitutively-expressed or Cre-dependent (Fl) FAPpost and dTom, separated by a 2A sequence for independent localization. (B) Fl-YFPpost construct. Cre-dependent YFPpost and dTom expression. (C) Virus injection coordinates. (D) Confocal image stack of L2 Pyr cell transfected with FAPpost. Scale = 10µm. (E) Optical section of FAPpost puncta on soma of cell in *D*. Scale = 2µm. (F) Zoom of *F*. Arrow-head marks cytoplasmic FAPpost accumulation. Scale = 1µm. (G) FAPpost labeled spiny dendrites. Scale = 1µm. (H) *In vivo* 2P imaging schematic. (I) Single-plane 2P image of L2 Pyr cells transfected with of YFPpost and dTom. Scale=30µm. (J) Single-plane 2P image of YFPpost-labeled spiny dendrite in L1. Scale as in *D*+*G*. See also Movie 1.

Figure 2. FAPpost synaptic localization does not alter mEPSC and mIPSC properties. (A) Example voltage-clamp traces from an untransfected (black) and neighboring FAPpost-expressing (red) L2/3 Pyr cell showing mEPSCs. (B) Comparison of mean mEPSC frequency ($ANOVA_{Frequency}$: $F_{(1,16)}$=0.2, p=0.6) and amplitude ($ANOVA_{Amplitude}$: $F_{(1,16)}$=0.1, p=0.8) indicate no difference. (C) Cumulative distribution histogram of mEPSC amplitudes (Kolmogorov-Smirnov Test, D=0.05, p=0.16). (D) Example voltage-clamp traces from an untransfected (black) and neighboring FAPpost-expressing (red) L2/3 Pyr cell showing mIPSCs. (E) Mean mIPSCs frequency (left) of untransfected and dTom cells were not significantly different ($ANOVA_{Frequency}$: $F_{(1,18)}$=0.6, p=0.4). Mean mIPSC amplitude (right) of untransfected and dTom cells were not significantly different ($ANOVA_{Amplitude}$: $F_{(1,18)}$=0.5, *p*=0.5). (F) Cumulative distribution histogram of mIPSC amplitudes shows a small but significant shift in dTom mIPSC amplitudes (Kolmogorov-Smirnov Test, D=0.15, p<0.0001). n=8-11 cells, N=7 animals.

946 **Figure 3. FAPpost puncta align with presynaptic bassoon.** (A) Optical section of a
947 confocal image used to assess bassoon immunofluorescence alignment with PV terminals on soma of
948 FAPpost labeled cell visualized in Ai3xPV-Cre mouse. Quadruple channel overlay showing
949 presynaptic PV terminal (YFP, cyan) colocalization with bassoon immunofluorescence (Alexa405;
950 yellow) and alignment with FAPpost puncta (green) on dTom (red) filled soma. Scale, 1µm. (B-E)
951 As in *A,* but each channel in isolation. White arrows indicate triple-channel alignment example
952 puncta, orange arrow indicates quadruple-channel alignment example puncta. (F) Presynaptic
953 bassoon puncta rate of alignment with FAPpost (F+) and/or colocalization with PV terminals (P+).
954 Bars are mean±SD of individual soma alignment rates (dots; n=5 soma; puncta assessed, n=104). (G)
955 FAPpost puncta rate of alignment with bassoon (B+) and/or PV terminals (P+; dots; n=5 soma;
956 puncta assessed, n=92). (H) PV terminal rate of alignment with FAPpost (F+) and colocalization with
957 bassoon (B+, dots; n=5soma, terminals assessed, n=83). (I) Triple channel overlay showing
958 presynaptic bassoon immunofluorescence (Alexa405; white) alignment with dendritic FAPpost.
959 Scale, 1µm. (J-L) As in *I,* but each channel in isolation. White arrowhead indicates FAPpost puncta
960 not aligned with bassoon. (M) FAPpost rate of alignment with bassoon (B+) along separate dendritic
961 segments (dots; n=11 dendritic segments; puncta assessed, n=143).

962 **Figure 4. Synapse quantitation for L2/3 Pyr neurons.** (A) Confocal stack of example
963 FAPpost Pyr neuron. (B) Zoom of spiny dendritic segment. (C) Schematic for dendritic puncta
964 assignment (green, assigned puncta $\leq$1.0µm from shaft surface; light green, unassigned puncta).
965 (D+E) 3D-rendering of the neuron and puncta assignment. Scale = 10 µm, 2 µm. (F) Schematic of
966 Pyr branch orders analyzed. (G) Mean FAPpost puncta density for individual neurons (grey
967 bars,$\pm$SEM) on 2°-4° apical and 1°-4° basal dendritic branches (black dots). (H) Somatic and
968 dendritic puncta density are correlated (R^2=0.37, *p*=0.0003). (I) Mean FAPpost synapse density
969 across 1°-4° Pyr branches (bar$\pm$SEM). (right) Individual cell values, plotted as connected lines. RM

41

970 $ANOVA_{Pyr}$: $F_{(7,126)}=19$, $p<0.0001$. All data shown (n=29 cells, N=12 animals), statistical
971 comparisons performed on balanced data (n=19 cells, N=10 animals). See Extended Data Figure 4-1
972 for puncta detection using YFPpost and Extended Data Figure 4-2 for Imaris analysis workflow.

973 **Figure 5. FAPpost puncta on the primary apical dendrite align with presynaptic PV**
974 **neurites.** (A) Six serial optical sections of a Pyr primary apical dendrite labeled with FAPpost
975 (green) and dTom (red). (Top row) Fluorescence aligned with presynaptic PV (YFP; cyan). (Bottom
976 row) FAPpost and dTom fluorescence alone. (B) Flattened stack of the region in *A,* showing
977 PV(YFP) and dTom. (C) Rendering of *B.* (D) As in *B*, but for FAPpost and dTom. (E) Rendering of
978 PV-assigned FAPpost puncta (large red balls) and unassigned (small green balls) puncta. Scale=1µm.

979 **Figure 6. FAPpost detection improves estimates of input association.** (A) Diagram
980 illustrating distance parameters used for FAPpost puncta assignment to soma-surface (left), soma-
981 puncta association with presynaptic YFP-expressing neurites (middle), and presynaptic neurite
982 associations with soma-surface (right). (B) Comparison of the number of presynaptic neurite to
983 soma-surface and soma-puncta associations. Connected lines = individual cell values. More PV
984 neurite to PYR soma-surface (115±16) than soma-puncta contacts were detected (66±30; Paired T-
985 Test, t=3.3, p=0.01). More SST neurite to soma-surface (69±10) than soma-puncta contacts were
986 detected (15±8; Paired T-Test, t=6.7, p=0.0001). Number of VIP neurite to soma-surface (16±4) and
987 soma-puncta contacts were similar (11±5; Paired T-Test, t=1.1, p=0.3). (C) Contact overestimation
988 depicts the difference between presynaptic neurite to soma-surface and soma-puncta associations for
989 presynaptic PV neurites (+49±15), SST neurites (+54±8), and VIP neurites (+5±4). Negative values
990 occurred when multiple puncta associated with a single presynaptic terminal. (D) Error rate for
991 presynaptic neurite-to-soma associations versus soma puncta associations for PV (115±56%), SST
992 (394±70%), and VIP inputs (280±162%). Across PYR cells, the percentage overestimation did not
993 vary by input cell type ($ANOVA_{CellType}$: $F_{(2,24)}=1.7$, p=0.2). PV input: n=9 cells, N=4 animals; SST

994 input: n=9 cells, N=4 animals; and VIP input: n=9 cells, N=3 animals. (E) Optical section of a
995 confocal image used to assess bassoon immunofluorescence alignment with PV terminals on soma of
996 FAPpost labeled cell visualized in Ai3xPV-Cre mouse. Scale, 2µm. (F) Boxed region from *A*,
997 quadruple channel overlay showing presynaptic PV terminal (YFP, cyan) colocalization with bassoon
998 immunofluorescence (Alexa405; yellow) and alignment with FAPpost puncta (green) on dTom (red)
999 filled soma. Scale, 0.5µm. (G-I) Same as B, but for PV, bassoon, and FAPpost visualized with dTom.
1000 (J) Presynaptic bassoon puncta rate of alignment with FAPpost (F+) and/or colocalization with PV
1001 terminals (PV+). Bars are mean±SD of individual soma alignment rates (dots; n=5 soma).

1002 **Figure 7. The distribution of PV, SST, and VIP inputs across L2 Pyr neurons.** (A) PV-
1003 input assigned synapses for an example L2 Pyr neuron. Small light-green spheres are un-assigned
1004 FAPpost puncta; large colored spheres are input-assigned FAPpost puncta. See Figure 7-1 for images
1005 of all input-analyzed Pyr neurons. (B) Mean density of PV-assigned FAPpost contacts across
1006 dendritic branch orders. (left) Bar is mean+SEM of all cells; (right) Individual cell values, plotted as
1007 connected lines. All data shown, statistical comparisons performed on balanced data. PV-assigned
1008 puncta density was greater for the 1° apical dendrite. RM $ANOVA_{PV\text{-}Input}$: $F_{(7,28)}=6.7$, $p=0.002$; n=5
1009 cells, N=3 animals. *Tukey post-hoc pairwise comparison test, $p<0.05$. (C) As in *A* but for SST. See
1010 Figure 7-2 for images of all input-analyzed Pyr neurons. (D) SST-assigned puncta density was not
1011 statistically significantly different across branch orders. RM $ANOVA_{SST\text{-}Input}$: $F_{(7,28)}=0.63$, $p=0.7$;
1012 n=5 cells, N=3 animals. (E) As in *A* but for VIP. Scale=20 µm. See Figure 7-3 for images of all
1013 input-analyzed Pyr neurons. (F) VIP-assigned puncta density was greater for the 1° apical dendrite.
1014 RM $ANOVA_{VIP\text{-}Input}$: $F_{(7,42)}=3.8$, $p=0.003$; n=7 cells, N=3 animals. *Tukey post-hoc pairwise
1015 comparison test, $p<0.05$. (G) Inhibitory innervation of Pyr neurons, expressed as a percent of the total
1016 number of detected synapses, for each input source. All dendritic compartments pooled for somatic
1017 and dendritic comparison. Two-Way RM $ANOVA_{Input:}$ $F_{(2,24)}=45$, $p<0.001$. All * show Tukey post-
1018 hoc pairwise comparison test, $p<0.05$. (H) Pie-chart showing average proportion of input-assigned

43

1019 FAPpost contacts versus total detected synapses, binned as perisomatic (soma and 1° apical) or
1020 higher-order dendritic compartments (apical 3°+4° and basal 3°+4°). A greater proportion of PV-
1021 inputs were found on soma and 1° apical dendrite than for SST- or VIP-inputs. At higher-order apical
1022 branches, the proportion of SST-input (10.5 ± 1.9%) was similar to PV-input (16.2 ± 1.9%), but
1023 significantly greater than VIP-inputs (1.4 ± 1.9%). For higher-order basal branches, all input sources
1024 were significantly different (PV = 17.3 ± 1.4%, n=7 cells, N=4 animals; SST=10.2±1.4%, n=7 cells,
1025 N=4 animals; VIP = 2.3±1.4%, n=7 cells, N=2 animals). Two-Way RM $ANOVA_{Binned\text{-}Input}$: $F_{(2,18)}$=
1026 47.3, p<0.0001.

1027 **Movie 1. L2/3 Pyr neuron labeled with dTom and FAPpost.** Confocal image stack of an
1028 isolated L2/3 neuron with pyramidal morphology showing punctate FAPpost (pseudocolored green)
1029 along the soma and dendritic arbor.

1030 **Table 1. Experimental metadata.**

1031 **Figure 4-1. YFPpost fluorescent puncta quantitation in L2/3 Pyr cell dendrites.** (A) Sparse
1032 YFPpost expression across the cortical column. Scale=50 µm. (B) L2/3 Pyr expressing YFPpost. (C)
1033 YFPpost fluorescent puncta on a dendritic shaft and spines (zoom from box in *B*). (D) Schematic for
1034 dendritic puncta assignment (blue, assigned puncta ≤1.0µm from shaft surface; light blue, unassigned
1035 puncta). (E) 3D-rendering of Pyr neuron (red) with assigned puncta. Scale=20µm. (F) Dendrite
1036 from *C* with assigned puncta. Scale=2µm. (G) Mean YFPpost puncta density for individual neurons
1037 (grey bars,+SEM) on apical and basal dendritic branches (black dots). n=21 cells, N=4 animals. See
1038 also Figure 4-2 and Table 1.

1039 **Figure 4-2. Fluorescent puncta detection method using Imaris.** (A) Image files imported
1040 into Imaris. Scale=40µm. (B) Raw synaptic fluorescent signal. (C) Gain-adjusted view of synaptic
1041 fluorescent signal to visualize dim YFP signal. (D) White mask of synaptic fluorescence
1042 differentiates signal from background. (E) Puncta creation parameters: 0.5 µm estimated diameter,
1043 larger than 3 voxel size (grey pixels). (F) 3D-renderings of all fluorescent puncta (yellow). (G)

1044 Puncta within 0.5 µm from cell surface (edge-to-edge; blue). (H) Isolated cell-associated puncta
1045 (blue). (I+J) Cytoplamic puncta (≤ 0.5 µm from cell surface; yellow). Scale=5µm. (K+L) Isolated
1046 cell-surface puncta. (M) Raw synaptic fluorescence used for Imaris spot detection. (N) Local
1047 fluorescence intensity maxima identified using automatic detection parameters (yellow spots). (O)
1048 3D-rendering of puncta centers (from *L)* as spots. (P+Q) Alignment of puncta 3D-renderings and
1049 spots. Scale=1µm. (R) Alignment of spots and signal enhanced fluorescence. (S+T) Alignment of
1050 spots and raw fluorescence. Scale=5µm. (U) Workflow summary.

1051 **Figure 7-1. PV-assigned FAPpost puncta distribution across Pyr cells.** Small light-green
1052 spheres are un-assigned FAPpost puncta. Large colored spheres are input-assigned FAPpost puncta.
1053 Scale=15µm.

1054 **Figure 7-2. SST-assigned FAPpost puncta distribution across Pyr cells.** Small light-green
1055 spheres are un-assigned FAPpost puncta. Large colored spheres are input-assigned FAPpost puncta.
1056 Scale=15µm.

1057 **Figure 7-3. VIP-assigned FAPpost puncta distribution across Pyr cells.** Small light-green
1058 spheres are un-assigned FAPpost puncta. Large colored spheres are input-assigned FAPpost puncta.
1059 Scale=15µm.

45

Fig1

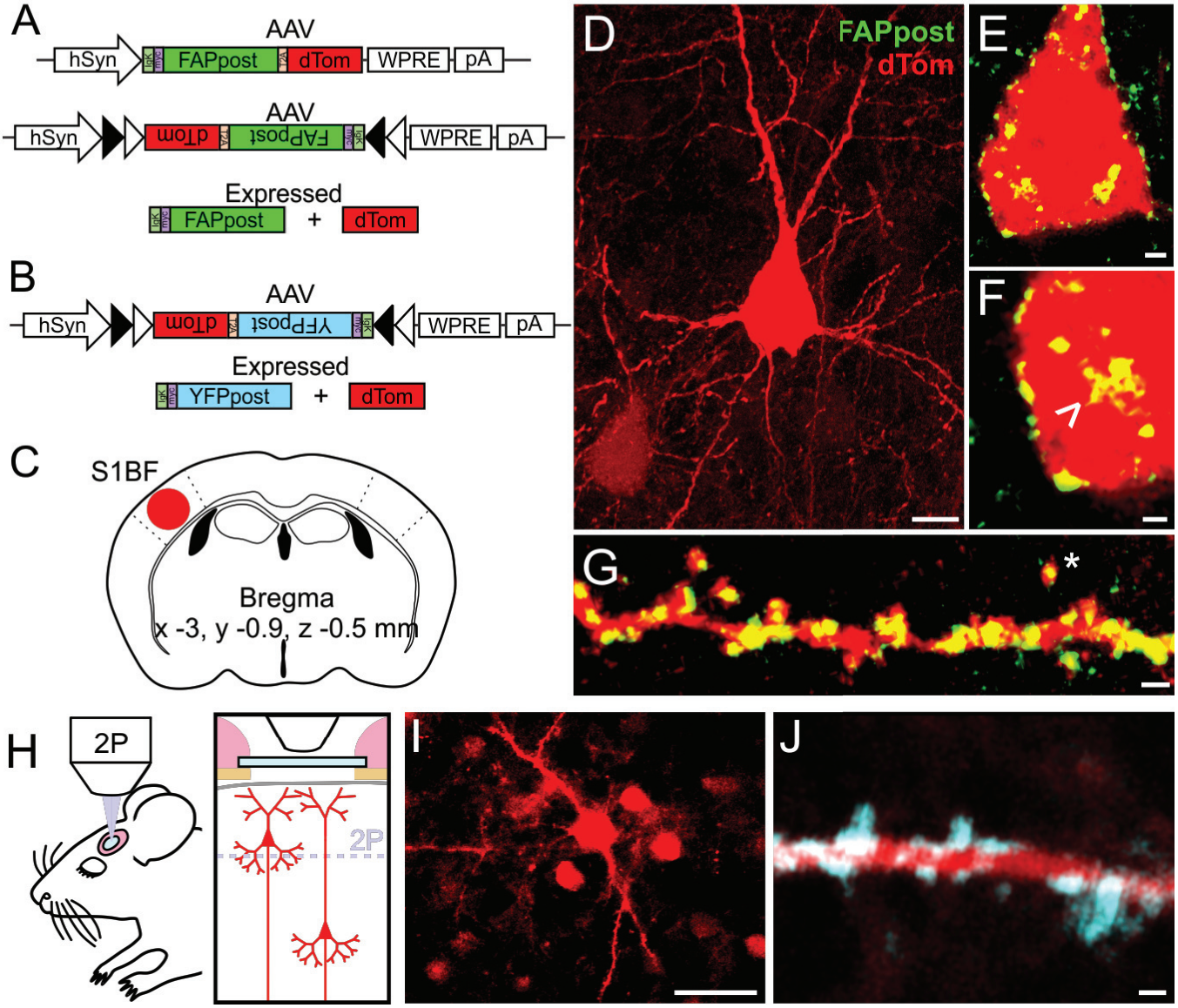

Fig2

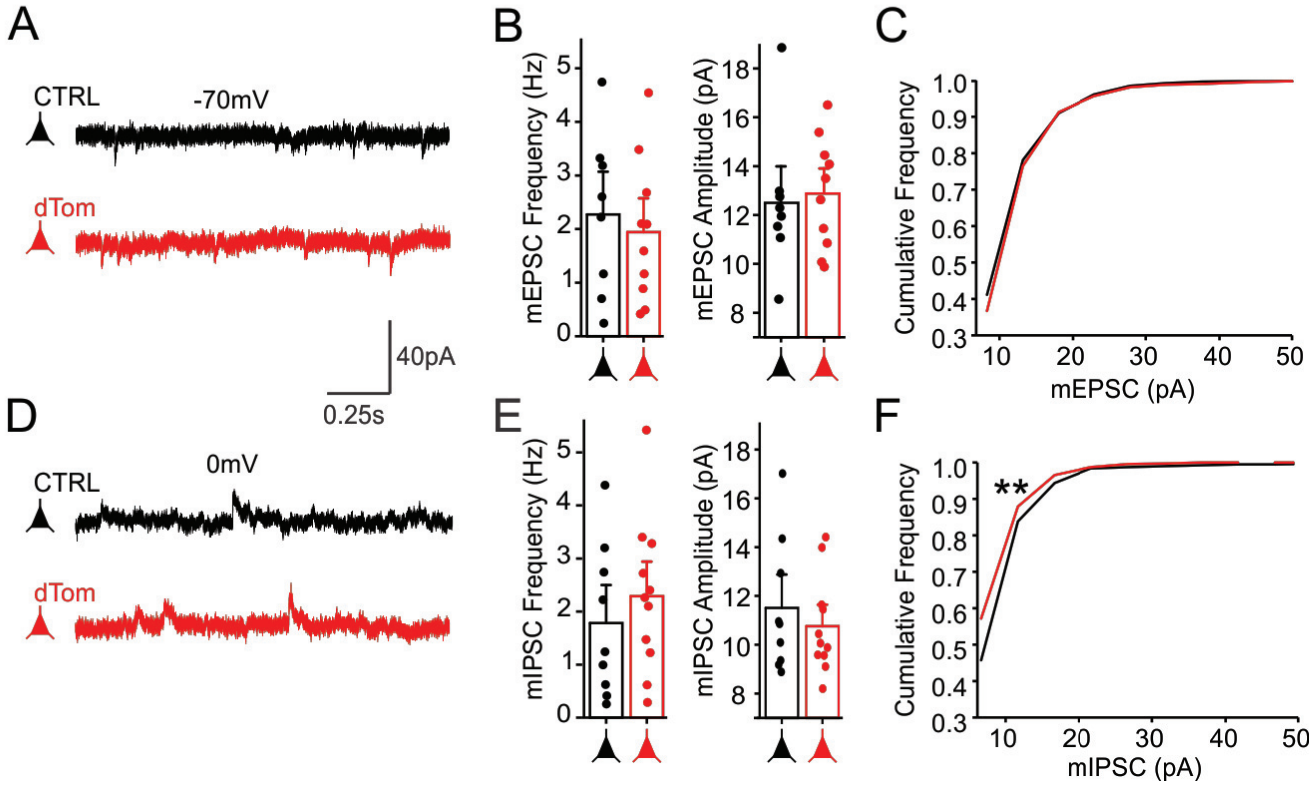

Fig3

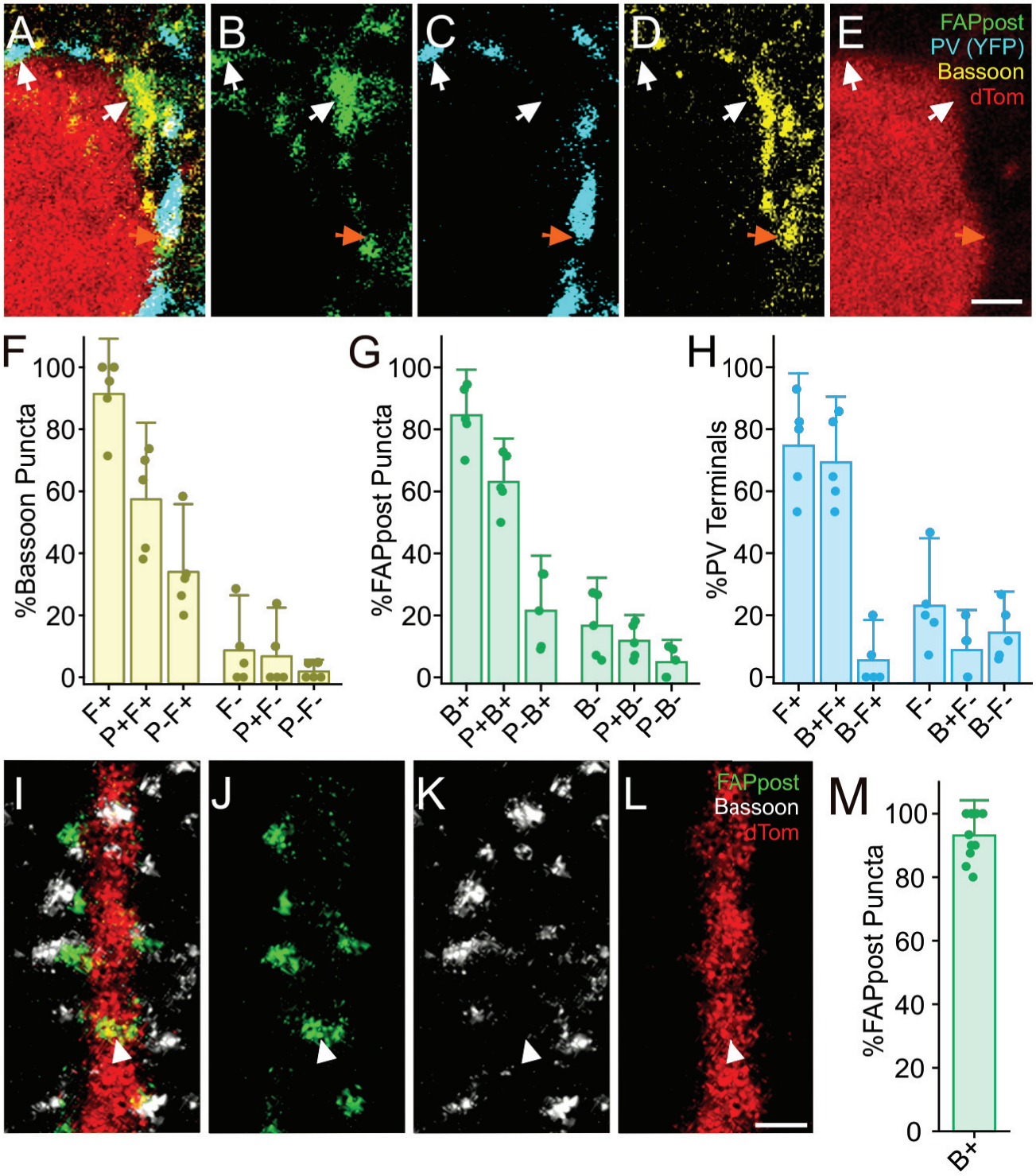

Fig4

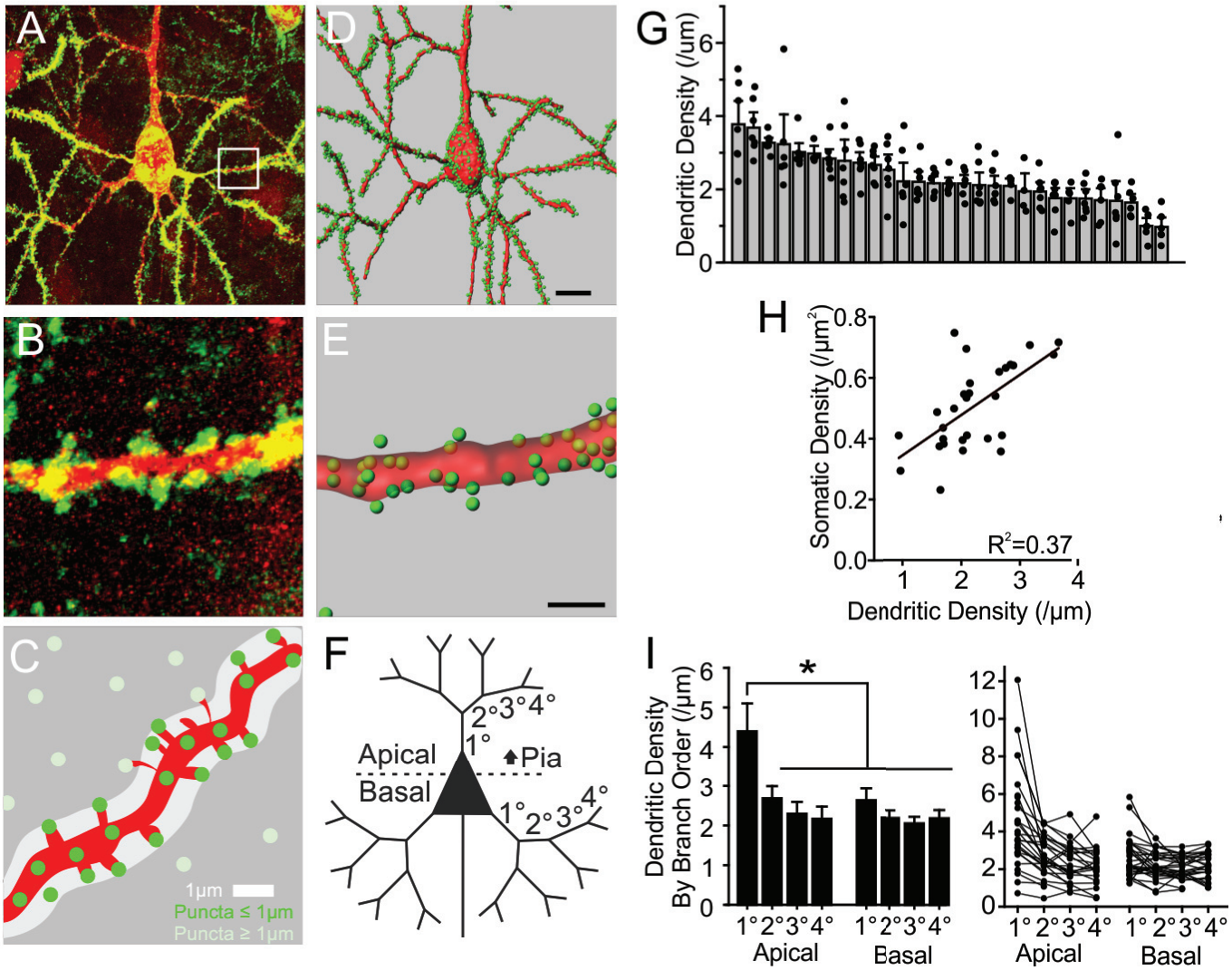

Fig5

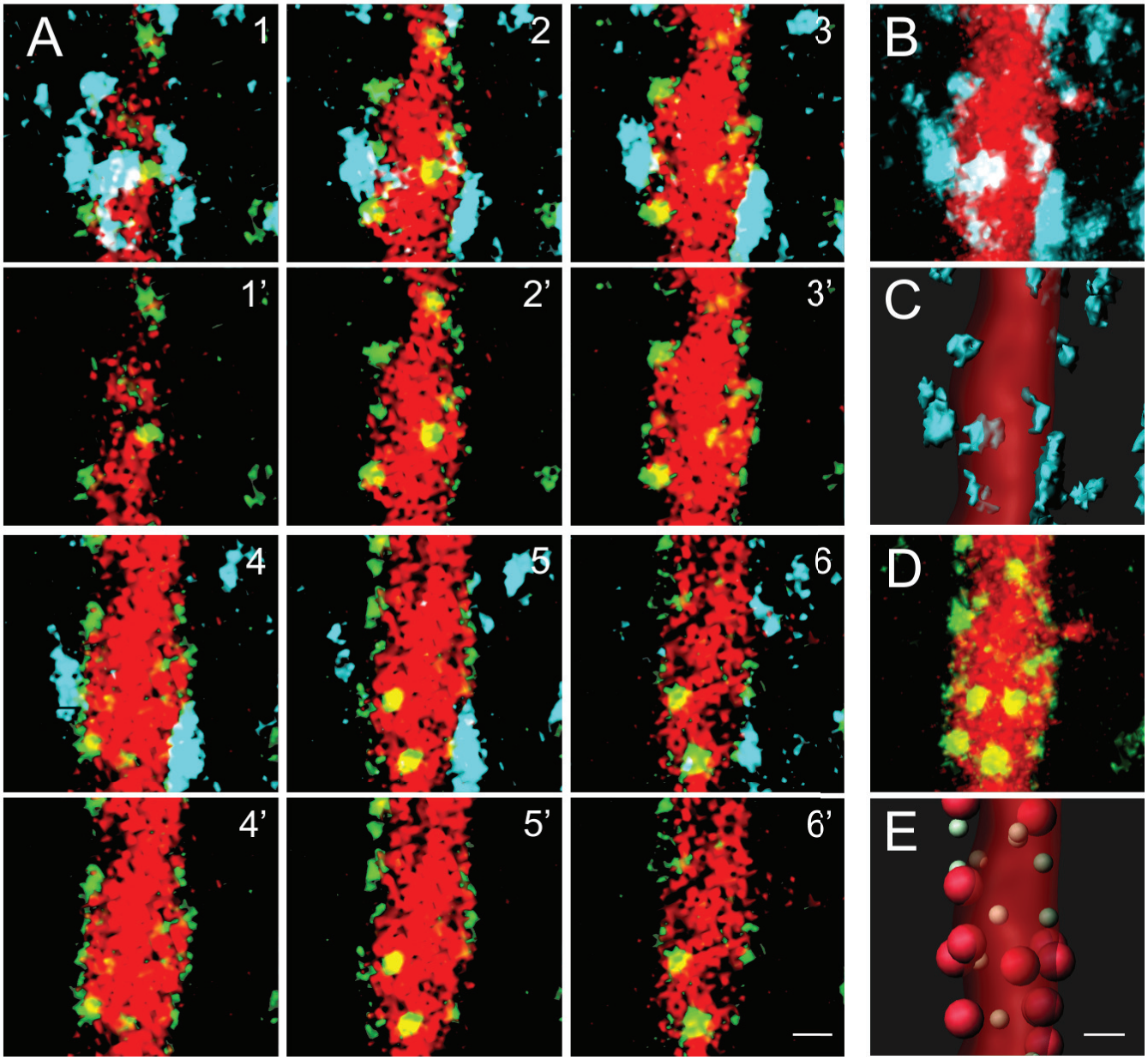

Fig6

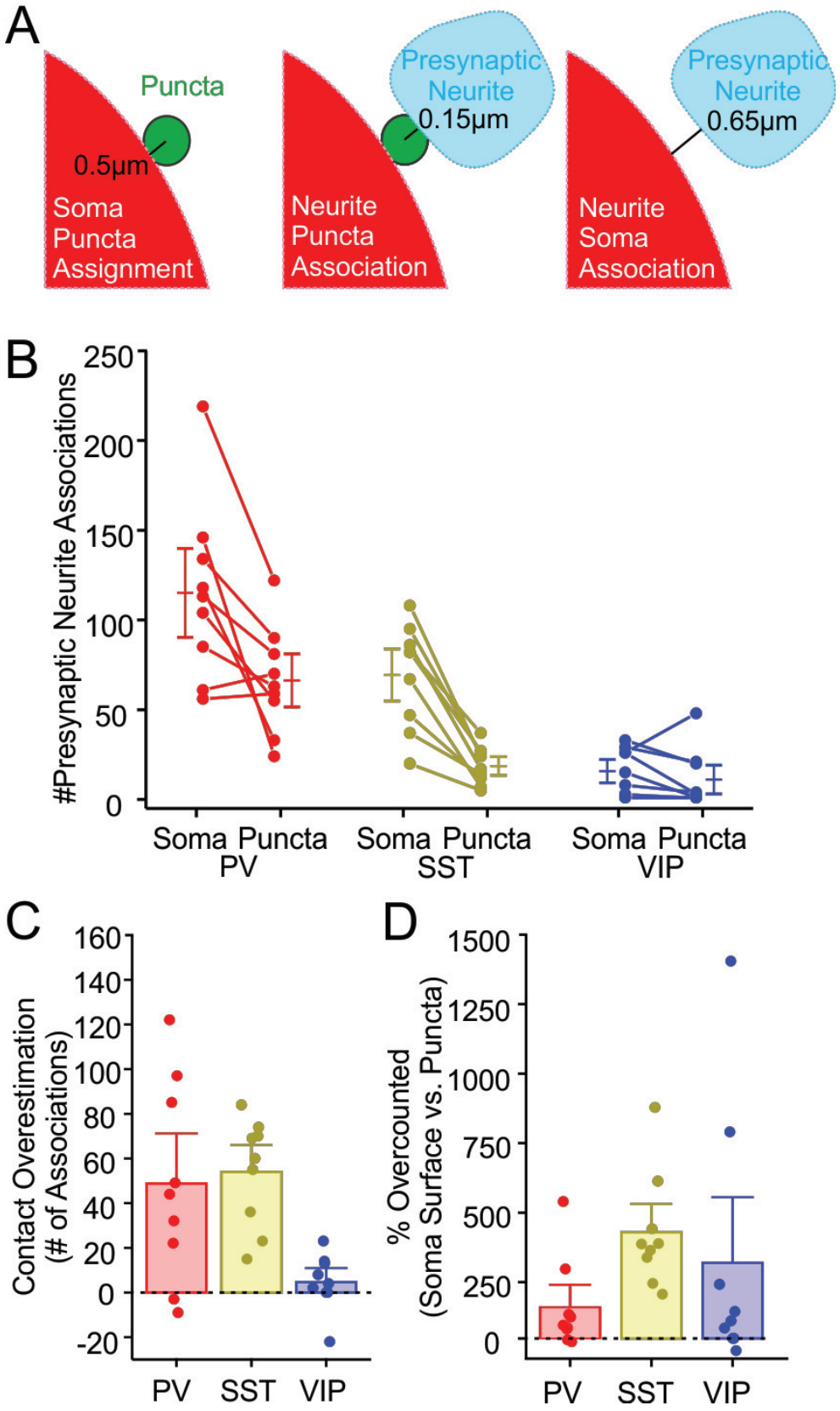

Fig7

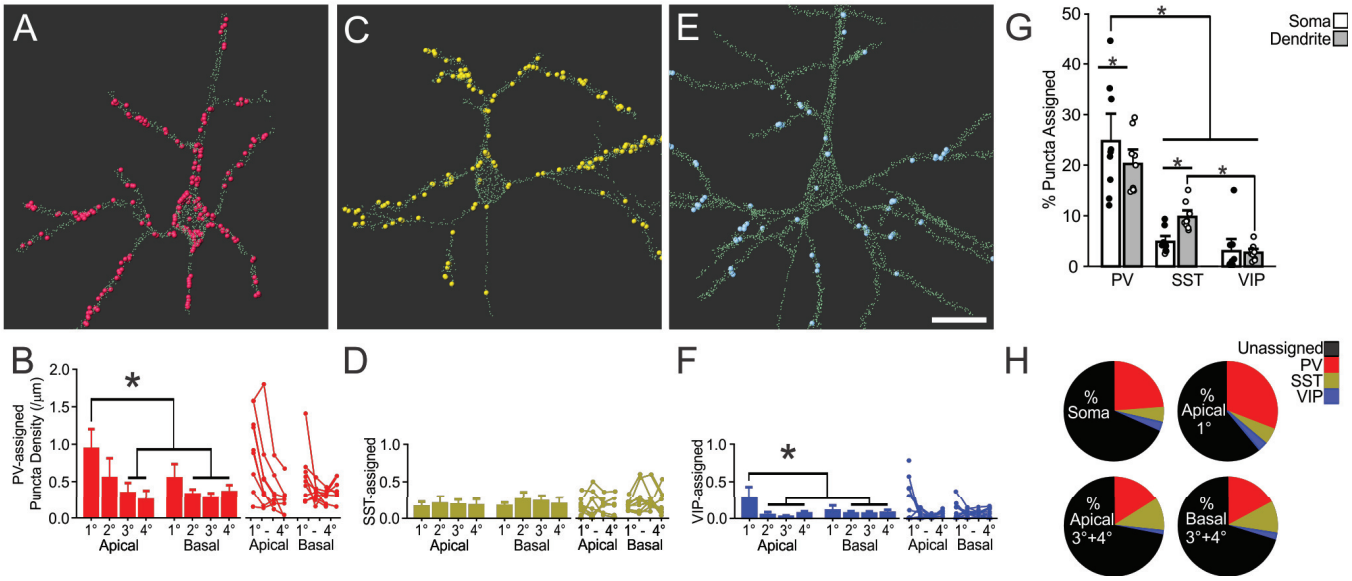

Table 1. Experimental metadata

Cell Type	Contruct	Animal ID	Sex	Cell ID	Genotype	Age	DPI	n =	Mean ± SEM
Pyr	FAPpost	BZS1	M	5, 11, 12	Ai3xVIP-Cre	24	9	3	3.40 ± 0.32
		BPP8	F	1, 11	Ai3xPV-Cre	24	11	2	1.38 ± 0.38
		BZS3	M	2, 3, 4, 5	Ai3xVIP-Cre	25	10	4	2.93 ± 0.13
		BQW1	M	11	Ai3xSST-Cre	25	11	1	2.15 ± NA
		BQW4	F	6, 10, 11, 12	Ai3xSST-Cre	25	11	4	2.09 ± 0.17
		BXT6	M	1, 2	Ai3xSST-Cre	25	8	2	2.08 ± 0.14
		BYS1	F	1, 3	Ai3xSST-Cre	26	9	2	1.32 ± 0.36
		BLN11	F	17	Ai3xPV-Cre	27	15	1	2.78 ± NA
		BFE4	M	2, 10	WT	27	13	2	2.18 ± 0.02
		BLN7	F	6, 7	Ai3xPV-Cre	27	15	2	1.67 ± 0.03
		BLW4	F	43, 45	Ai3xVIP-Cre	28	14	2	2.53 ± 0.44
		CHI3	F	3, 4, 5, 9	Ai3xPV-Cre	28	12	4	2.17 ± 0.21
	YFPpost	CPV1	F	1, 3, 4	Emx1-Cre	22	7	3	2.77 ± 0.15
		CNH4	M	1, 2, 4, 5, 6, 7, 8	Emx1-Cre	24	10	7	2.98 ± 0.24
		CNH5	F	2, 3, 4, 5, 6	Emx1-Cre	24	10	5	2.34 ± 0.06
		CPW1	F	1, 2, 3, 4, 5, 6	Emx1-Cre	27	10	6	3.21 ± 0.29